Computational Mechanics
https://doi.org/10.1007/s00466-024-02558-1

ORIGINAL ARTICLE

Mesh topology-based spurious pressure stabilization in 3D finite elasticity using Voronoi tessellations

Bjorn Sauren[1] · **Sven Klinkel**[1]

Received: 29 April 2024 / Accepted: 9 September 2024

Abstract
In this paper, we present a mesh topology-based stabilization approach to suppress spurious pressure modes in 3D nearly-incompressible finite elasticity. The focus lies on a mixed formulation with lowest-order approximation for the displacement and pressure fields. Motivated by the fact that the popular H1/P0 element does not fulfill the inf-sup condition, all possible local spurious pressure modes are derived on a patch of elements. The nullspace method is used to determine all spurious pressure solutions. From this, the topological requirements of the finite element mesh are established. We conclude that no more than four elements are allowed to intersect in the same vertex to overcome local checkerboarding. To fulfill this requirement, we employ non-degenerate 3D Voronoi diagrams with several different site distributions. These result in random, centroidal, and honeycomb Voronoi meshes. The resulting convex polyhedral elements are discretized by a polyhedral mixed finite element based on the lowest possible interpolation pair. The numerical examples illustrate that spurious pressure modes do not occur for any degree of mesh refinement as long as the topological mesh requirements are met. Furthermore, it is shown that the numerical inf-sup test is passed. By violating the topological requirements, it is shown that a stable pressure field cannot be guaranteed and the checkerboard phenomenon is provoked.

Keywords Spurious pressure · Checkerboard modes · Finite elasticity · Inf-sup · Voronoi mesh

1 Introduction

A well-posed solution to a minimization problem can usually be obtained by the irreducible form of the finite element method (FEM). The test and trial spaces are then constrained by necessary boundary conditions. Within some specific problems, the solution is subjected to additional constraints. These are essential in numerous applications in computational solid and fluid mechanics and have to be considered accurately. In this contribution, we investigate the limiting case of (nearly-)incompressible (hyper)elasticity, in which the constraint enforces a divergence-free displacement field in linear analysis, and velocity field in nonlinear analysis, respectively [1]. Other examples can be found within the field of topology optimization, where constraints are typically imposed on material densities and volume fractions [2], or in contact mechanics, where the minimization problem is solved with respect to a contact constraint [3].

The incompressibility constraint can be incorporated into a finite element formulation in either a strong or weak manner. A strong imposition of the constraint *a priori* necessitates the construction of a new finite element space. These so-called divergence-free finite element formulations are studied and developed in recent works [4, 5], however, are applied to problems in computational fluid dynamics almost exclusively. In computational solid mechanics, this approach is rather unconventional. Alternatively, the constraint can be enforced by a sufficiently large penalty parameter (i.e. the bulk modulus), however, this approach has an unfavorable impact on the well-posedness of the problem [3]. When considering an incompressible solid, the infinitely large bulk modulus results in a singular compliance tensor and consequently, no solution can be found. In the somewhat less restrictive nearly-incompressible case, a solution can be found but will be severely underestimated. This phenomenon is called volumetric locking. Due to these drawbacks, one

---

We dedicate this paper to Jörg Schröder on the occasion of his 60th birthday.

✉ Bjorn Sauren
sauren@lbb.rwth-aachen.de

[1] Chair of Structural Analysis and Dynamics, RWTH Aachen University, Mies-van-der-Rohe-Str. 1, 52074 Aachen, Germany

would rather refrain from reducing the finite element space or the use of a penalty parameter and impose the incompressibility constraint differently. The most common approach is the introduction of a Lagrange multiplier, which transforms the minimization problem into a saddle-point problem. In the framework of the FEM, it is then necessary to approximate both the primal solution field and the Lagrange multiplier independently. These methods, known as mixed finite element methods, have shown to be effective in retaining the well-posedness of the problem and contribute to the alleviation of locking. Mixed finite element formulations are studied and developed in several recent contributions for (nearly-)incompressible problems in solid mechanics, see [6, 7]. These include displacement-pressure formulations for polygonal meshes, such as the formulations contributed by the authors [8, 9], Wriggers [10, 11], and others [12, 13]. Alternative formulations incorporate the displacement-pressure formulation into the material point method [14, 15]. In References [16–21], the Hellinger–Reissner functional is used to obtain volumetric locking-free stress-displacement formulations for solids. Moreover, it is possible to derive a mixed variational form using the Hu–Washizu potential [22, 23], which alleviates locking in the lowest-order element formulation.

The well-posedness of the solution to a mixed finite element problem is related to the discrete finite element spaces used to approximate each individual field. In this context, two conditions are of importance: the coercivity condition and the inf-sup (or LBB) condition. While coercivity is generally fulfilled quite easily, the inf-sup condition requires a more thorough consideration. This condition, proposed by Ladyzhenskaya [24], Babuška [25], and Brezzi [26], defines the necessary condition to guarantee existence and uniqueness of the solution. Analytical inf-sup proofs for popular mixed finite elements can be found in various finite element textbooks (see e.g. [27]), however, are limited to linear analysis. During the development of new mixed element formulations, the numerical inf-sup test [28] presents a valuable alternative to the sometimes cumbersome analytical derivation. The simplicity of the inf-sup test has caused it to become a standard tool for engineers. Both approaches indicate that the Q1/P0 element (2D) and H1/P0 element (3D) do not fulfill the inf-sup condition. As a result, these elements could provide a meaningless pressure solution while the displacement solution is generally stable, sufficiently accurate and volumetric locking-free. Extending this theory to analyze nonlinear problems remains a complex task. While it is possible to evaluate the condition for the tangent space of the discrete problem, all possible intermediate displacement and pressure states must be covered. A numerical procedure to assess the stability of nonlinear elements, extending the theory presented in [28], is presented in [29]. It can be used to obtain an estimate on whether or not a new nonlinear mixed finite element fulfills the inf-sup condition.

The aforementioned pressure instability in the Q1/P0 and H1/P0 elements is generally expressed as a spurious pressure mode. Its cause is well-understood and reported [30]. Different remedies can be employed in several stages of numerical analysis. Postprocessing techniques, which include smoothing [31] or filtering [32] of the pressure field, are effective on regular finite element meshes. During the finite element calculation, one can use stabilized mixed finite element formulations to circumvent or fulfill the inf-sup condition. Noteworthy stabilization techniques for equal-order approximations include the variational multiscale method (VMS) [33, 34] or subdivision stabilized mixed formulations for B-splines [35]. Alternatively, enriched mixed finite element formulations [36, 37] can be used to overcome spurious pressure solutions. Another possibility is an order elevation of both the displacement and pressure interpolation functions. The resulting $\mathrm{Q}_i/\mathrm{P}_{i-1}$ elements with $i \geq 2$, or Taylor–Hood elements [38], fulfill the inf-sup condition and yield well-posed pressure solutions. Whereas the solution will be more accurate than the Q1/P0 element on coarse meshes, its numerical effort is higher. This is caused by the increasing number of degrees-of-freedom per element, especially those corresponding to the bilinear pressure approximation and its continuity across element boundaries. In contrast to elements with a constant pressure, these continuity requirements do not allow for static condensation of the pressure degrees-of-freedom on element level, requiring the nodal pressures to be solved accordingly. Moreover, the authors have shown that one can change the mesh topology *a priori* to suppress spurious pressure modes in two-dimensional finite elasticity [39], which generalizes the theory presented in [40]. It is shown that the physical hydrostatic pressure mode is the only pressure mode that can occur on a Voronoi mesh.

In this article, the aforementioned considerations are extended to three-dimensional solids undergoing large and nearly-incompressible deformations. The general framework of our discussion is a linear displacement–constant pressure element in three-dimensional space. Whereas spurious pressure modes are somewhat manageable and treatable by the aforementioned techniques on quadrilateral meshes, the number of spurious modes increases drastically if a hexahedral or tetrahedral mesh is considered. We show that the occurrence of spurious pressure modes in three dimensions is inherently concerned with the number of finite elements connected to a vertex. Using the nullspace method, all possible spurious pressure modes are determined on a patch of elements at an arbitrary displacement state. From this, we conclude that the suppression of spurious pressure modes is possible if no more than four finite elements intersect in the same vertex. It is subsequently shown that, due to the characteristics of a non-degenerate Voronoi mesh, no more than four Voronoi elements coincide in a vertex and the criterion is thus fulfilled. Based on an exemplary patch of Voronoi elements, we show analytically that the only possible pressure mode is purely hydrostatic and is thus physical. All derivations are based on the nonlinear weak formulation and can be evaluated in the undeformed configuration to consider linear problems.

Due to the polyhedral geometry of the Voronoi elements, appropriate mixed finite element formulations are necessary to discretize the weak formulation. Similar to [8] and [41], the Voronoi elements are discretized by a fully numerical mixed scaled boundary finite element formulation. By inserting a single scaling center in the interior of each element, the faces of a polyhedron can be scaled along the scaling direction. The assumed constant pressure in a polyhedral element alleviates locking (see [8]) and will become an essential aspect in this article to avoid spurious pressure modes.

Two benchmarks are used to demonstrate that a stable pressure field can be guaranteed if the appropriate mesh topology is chosen. In each problem, the pressure distribution is visualized on at least two types of meshes. It is shown that these are (sometimes heavily) polluted by spurious pressure modes if discretizations are chosen that do not fulfill the topological requirements. On the other hand, all results evaluated on non-degenerate 3D Voronoi meshes are stable and deliver smooth pressure solutions. Moreover, the simplicity of the Voronoi algorithm allows us to construct multiple mesh configurations that fulfill the necessary topological requirements. These include random, centroidal, or honeycomb Voronoi tessellations.

The article is subdivided into five sections. In Sect. 2, the incompressibility constraint and its incorporation into the FEM are discussed. The necessary terminology and stability criteria are stated. The nullspace of the stiffness matrix is derived at an arbitrary interior mesh vertex in Sect. 3. The allowed number of intersecting elements is derived. It is shown briefly that Voronoi meshes possess the necessary properties. Numerical results are shown in Sect. 4, a summary of this work is given in Sect. 5.

2 Constrained minimization

2.1 Variational formulation

In this work, we consider a (hyper)elastic body $\mathcal{B}$ occupying a bounded continuum domain $\Omega = \Omega_0 \subset \mathbb{R}^3$ in an undeformed configuration at $t = 0$ (Fig 1a). Its boundary $\partial\Omega = \partial\Omega_D \cup \partial\Omega_N$ consists of a Dirichlet boundary $\partial\Omega_D \subset \mathbb{R}^2$ and a Neumann boundary $\partial\Omega_N \subset \mathbb{R}^2$. The material is assumed to be hyperelastic and isotropic. These assumptions allow us to define a strain energy density function, which may be decomposed additively as

$$\begin{aligned} W(\mathbf{C}, J) &= W_{\text{dev}}(\mathbf{C}) + W_{\text{vol}}(J) \\ &= W_{\text{dev}}(\mathbf{C}) + \frac{\kappa}{2}\left[\hat{U}(J)\right]^2. \end{aligned} \tag{1}$$

The deviatoric part $W_{\text{dev}}(\mathbf{C})$ defines the strain energy density function related to all volume-preserving deformation modes. The strain energy density function $W_{\text{vol}}(J)$ contributes to volume change. It scales linearly with the bulk modulus κ. The penalty function $\hat{U}(J)$ is commonly of the form

$$\hat{U}(J) = J - 1. \tag{2}$$

In Eq. (1), $\mathbf{C} = \mathbf{F}^{\mathsf{T}}\mathbf{F}$ denotes the right Cauchy-Green deformation tensor, which consists of the deformation gradient $\mathbf{F} = \mathbf{I} + \text{Grad}(\mathbf{u})$ with $J = \det(\mathbf{F})$. Here, $\text{Grad}(\mathbf{u})$ defines the gradient of the displacement vector $\mathbf{u}$ with respect to the Cartesian reference frame in the undeformed configuration at $t = 0$.

The internal energy Π_{int} and external energy Π_{ext} stored in or acting on Ω are considered. The total potential energy reads

$$\begin{aligned} \Pi(\mathbf{u}) = &\underbrace{\int_\Omega W(\mathbf{C}, J)\, \mathrm{d}V}_{\Pi_{\text{int}}(\mathbf{u})} \\ &- \underbrace{\left(\int_\Omega \mathbf{u}\cdot\mathbf{f}\, \mathrm{d}V + \int_{\partial\Omega_N} \mathbf{u}\cdot\bar{\mathbf{t}}_0\, \mathrm{d}A\right)}_{\Pi_{\text{ext}}(\mathbf{u})}, \end{aligned} \tag{3}$$

where the body force vector is denoted by $\mathbf{f}$ and the initial boundary traction vector is given by $\bar{\mathbf{t}}_0$. A unique minimizer $\mathbf{u} \in \mathcal{H}_0^1(\Omega)$ of $\Pi(\mathbf{u})$ is sought by variation of all kinematically admissible functions $\delta\mathbf{u} \in \mathcal{H}_0^1(\Omega)$ as

$$\mathbf{u} = \arg \inf_{\delta\mathbf{u}\in\mathcal{H}_0^1(\Omega)} \Pi(\delta\mathbf{u}). \tag{4}$$

Here, $\mathcal{H}_0^1(\Omega)$ is a Hilbert space in $\mathbb{R}^3$ with imposed homogeneous Dirichlet boundary conditions on $\partial\Omega_D$. In order to find a solution to the minimization problem of Eq. (4), the equivalent variational formulation is defined:

Find $\mathbf{u} \in \mathcal{H}_0^1(\Omega)$ such that

$$\begin{aligned} \int_\Omega \delta\mathbf{E} : \frac{\partial W}{\partial \mathbf{E}}\, \mathrm{d}V = \int_\Omega \delta\mathbf{u}\cdot\mathbf{f}\, \mathrm{d}V + \int_{\partial\Omega_N} \delta\mathbf{u}\cdot\bar{\mathbf{t}}_0\, \mathrm{d}A \\ \forall\ \delta\mathbf{u} \in \mathcal{H}_0^1(\Omega). \end{aligned} \tag{5}$$

The tensor $\delta\mathbf{E} = \frac{1}{2}\left(\delta\mathbf{F}^{\mathsf{T}}\mathbf{F} + \mathbf{F}^{\mathsf{T}}\delta\mathbf{F}\right)$ with $\delta\mathbf{F} = \text{Grad}(\delta\mathbf{u})$ is denoted as the virtual Green-Lagrange strain. $\mathbf{S} = \partial W/\partial\mathbf{E}$

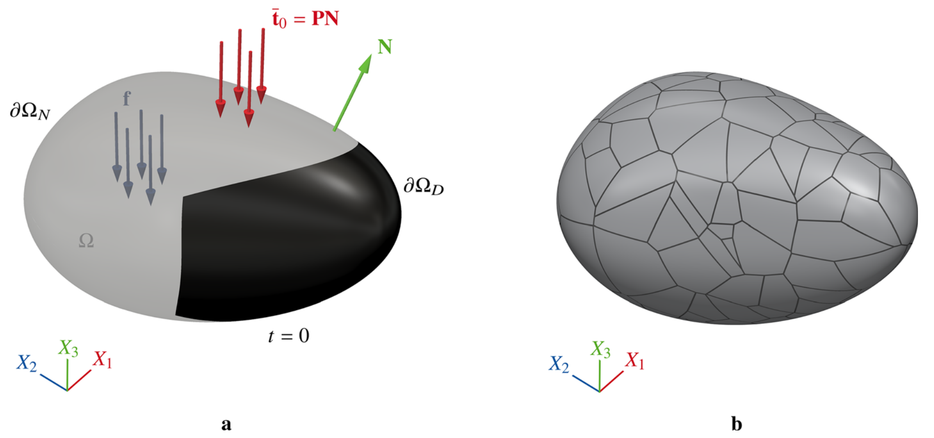

Fig. 1 **a** Hyperelastic and isotropic body $\mathcal{B}$ with tractions $\bar{\mathbf{t}}_0$, body forces $\mathbf{f}$ and material normal vector $\mathbf{N}$. **b** Random Voronoi tessellation of $\mathcal{B}$ using 150 Voronoi cells

defines the second Piola-Kirchhoff stress tensor. The boundary tractions equate to $\bar{\mathbf{t}}_0 = (\mathbf{FS})\mathbf{N}$, where $\mathbf{N}$ is the outward unit normal vector in the reference configuration.

2.2 Strong enforcement of the incompressibility constraint

The limiting case of incompressibility corresponds to the volume constraint in Eq. (2) being equal to zero and thus

$$J = 1. \tag{6}$$

As a result of this, there is no strain energy associated with volumetric compression or expansion of the body and consequently, $W_{\text{vol}} = 0$. Considering Eq. (1), the total strain energy is defined by the deviatoric part W_{dev} only:

$$\tilde{\Pi}(\mathbf{u}) = \int_{\Omega} W_{\text{dev}}(\mathbf{C}) \, \mathrm{d}V - \Pi_{\text{ext}}(\mathbf{u}) \,. \tag{7}$$

Still, the incompressibility constraint must be incorporated into the problem. Similar to imposing Dirichlet boundary conditions, the incompressibility constraint could be enforced on the solution space itself. The minimization problem yields:

$$\mathbf{u} = \arg \inf_{\delta\mathbf{u} \in \tilde{\mathcal{H}}_0^1(\Omega)} \tilde{\Pi}(\delta\mathbf{u}) \,, \tag{8}$$

with

$$\tilde{\mathcal{H}}_0^1(\Omega) := \left\{ \mathbf{v} \in \mathcal{H}_0^1(\Omega) \;\middle|\; \hat{U}(J) = 0 \right\}. \tag{9}$$

Constructing the space $\tilde{\mathcal{H}}_0^1(\Omega) \subset \mathcal{H}_0^1(\Omega)$ is cumbersome. We therefore aim for an equivalent formulation, which does not require a strong imposition of the incompressibility constraint on the finite element space explicitly.

2.3 Weak enforcement of the incompressibility constraint

The general and most common approach to fulfill the incompressibility constraint is the use of a Lagrange multiplier. The constraint is then incorporated weakly into the problem. Considering the penalty function of Eq. (2) with its corresponding Lagrange multiplier and appending their product to the potential of Eq. (7) yields

$$\Pi(\mathbf{u}, \; p) = \tilde{\Pi}(\mathbf{u}) + \underbrace{\int_{\Omega} p \, \hat{U}(J) \, \mathrm{d}V}_{\Pi_{\text{Lag}}(\mathbf{u}, \; p)} \,. \tag{10}$$

The Lagrange multiplier p enforces the incompressibility constraint and can be interpreted mechanically as the hydrostatic pressure. For nearly-incompressible problems, $J \approx 1$ applies, and the bulk modulus cannot be eliminated from the formulation. A perturbed Lagrangian is then used to enforce the constraint on the potential of Eq. (7), which becomes

$$\Pi(\mathbf{u}, \; p) = \tilde{\Pi}(\mathbf{u}) + \underbrace{\int_{\Omega} \left(p \, \hat{U}(J) - \frac{1}{2\kappa} p^2 \right) \mathrm{d}V}_{\Pi_{\text{Lag}}(\mathbf{u}, \; p)} \,. \tag{11}$$

In both cases, the stationary point of $\Pi(\mathbf{u}, \; p)$ corresponds to a saddle point. Equivalently to Eqs. (4) and (8), one still seeks for the minimizer over all admissible displacements. Simultaneously, the Lagrange multiplier corresponds to the maximizer of all pressures, and consequently:

$$(\mathbf{u},\ p)=\arg \inf_{\delta\mathbf{u}\in\mathcal{H}_0^1(\Omega)} \sup_{\delta p\in\mathcal{L}^2(\Omega)} \Pi\left(\delta\mathbf{u},\ \delta p\right). \qquad (12)$$

Here, $\mathcal{L}^2$ denotes the space of square-integrable functions with finite norm. It is easy to show that Eqs. (12) and (8) deliver equivalent results. That is, if $\hat{U}\left(J\right)\neq 0$, the supremum of the potential becomes infinite, which will never yield the minimum potential energy. In case of incompressibility and thus $\hat{U}\left(J\right)=0$, the supremum of the potential yields exactly Eq. (8). Note that the Hilbert space $\mathcal{H}_0^1\left(\Omega\right)$ now remains unchanged, while the constraint is fulfilled. The variational formulation corresponding to the saddle point problem becomes:

Find $(\mathbf{u},\ p)\in\mathcal{H}_0^1\left(\Omega\right)\times\mathcal{L}^2\left(\Omega\right)$ such that

$$\underbrace{\int_\Omega \delta\mathbf{E} : \frac{\partial W_{\text{dev}}}{\partial\mathbf{E}}\,\mathrm{d}V+\int_\Omega \delta\mathbf{E} : \frac{\partial\hat{U}}{\partial\mathbf{E}}\,p\,\mathrm{d}V}_{G_u}=\delta\Pi_{\text{ext}} \qquad (13a)$$

$$\forall\ \delta\mathbf{u}\in\mathcal{H}_0^1\left(\Omega\right)$$

$$\underbrace{\int_\Omega \delta p\ \hat{U}\left(J\right)\,\mathrm{d}V-\int_\Omega \delta p\ \frac{1}{\kappa}\ p\,\mathrm{d}V}_{G_p}=0 \qquad (13b)$$

$$\forall\ \delta p\in\mathcal{L}^2\left(\Omega\right).$$

In case of total incompressibility, the second term in Eq. (13b) vanishes. The $\mathcal{L}^2\left(\Omega\right)$-space allows the pressure to be discontinuous.

2.4 Linearization

The variational formulation in Eqs. (13) can be used to solve nonlinear problems. In order to obtain the solution to the displacement $\mathbf{u}$ and pressure p using a Newton–Raphson scheme, the problem must be linearized in the direction of their increments $\Delta\mathbf{u}$ and Δp as

$$\mathcal{D}_u G_u\cdot\Delta\mathbf{u}+\mathcal{D}_p G_u\cdot\Delta p=-G_u+\delta\Pi_{\text{ext}} \qquad (14a)$$

$$\mathcal{D}_u G_p\cdot\Delta\mathbf{u}\ -\mathcal{D}_p G_p\cdot\Delta p=-G_p. \qquad (14b)$$

While Eqs. (13) represent a non-symmetric system of equations, one can notice that the linearization in Eqs. (14) symmetrizes the problem. The directional derivatives read:

$$\mathcal{D}_u G_u\cdot\Delta\mathbf{u}=\int_\Omega \delta\mathbf{E} : \mathbb{C} : \Delta\mathbf{E}\,\mathrm{d}V+\int_\Omega \mathbf{S} : \Delta\delta\mathbf{E}\,\mathrm{d}V, \qquad (15a)$$

$$\mathcal{D}_p G_u\cdot\Delta p=\int_\Omega \delta\mathbf{E} : \frac{\partial\hat{U}}{\partial\mathbf{E}}\ \Delta p\,\mathrm{d}V, \qquad (15b)$$

$$\mathcal{D}_u G_p\cdot\Delta\mathbf{u}=\int_\Omega \delta p\ \frac{\partial\hat{U}}{\partial\mathbf{E}} : \Delta\mathbf{E}\,\mathrm{d}V, \qquad (15c)$$

$$\mathcal{D}_p G_p\cdot\Delta p=\int_\Omega \delta p\ \frac{1}{\kappa}\ \Delta p\,\mathrm{d}V, \qquad (15d)$$

where

$$\mathbb{C}=\frac{\partial^2 W_{\text{dev}}}{\partial\mathbf{E}\partial\mathbf{E}}+p\ \frac{\partial^2\hat{U}}{\partial\mathbf{E}\partial\mathbf{E}}, \qquad (16a)$$

and

$$\mathbf{S}=\frac{\partial W_{\text{dev}}}{\partial\mathbf{E}}+p\ \frac{\partial\hat{U}}{\partial\mathbf{E}}. \qquad (16b)$$

2.5 Mixed polyhedral finite element formulation

2.5.1 Approximation of the geometry

The reference domain Ω and its boundary $\partial\Omega$ are approximated using an arbitrary tessellation into n_E elements (Fig. 1b) and referred to as Ω_h and $\partial\Omega_h$, respectively. A particular element E (Fig. 2a) occupies a corresponding element domain $\mathcal{E}_E\subset\Omega_h\subset\mathbb{R}^3$ and thus

$$\Omega\approx\Omega_h=\bigcup_{E=1}^{n_E}\mathcal{E}_E. \qquad (17)$$

We refer to the boundary of the domain $\mathcal{E}_E$ as $\partial\mathcal{E}_E$. An element E must be at least tetrahedral, indicating that an element boundary $\partial\mathcal{E}_E$ is partitionable into a minimum of four and a maximum of n_F faces F (Fig. 2b). Each face occupies a planar domain $\mathcal{F}_F\subset\partial\mathcal{E}_E\subset\mathbb{R}^2$. It holds

$$\partial\mathcal{E}_E=\bigcup_{F=1}^{n_F}\mathcal{F}_F. \qquad (18)$$

Each planar face F is assigned a unique outward unit normal vector denoted $\mathbf{N}_F$. Omitting the definition of edges, the boundary $\partial\mathcal{F}_F$ of a face F consists of a minimum of three and a maximum of n_V vertices V. The position vector of a vertex V is denoted by $\mathbf{X}_V$. In the current configuration, we refer to the two- and three-dimensional domains by the superscript t, e.g. Ω_h^t, $\mathcal{E}_E^t$ and $\mathcal{F}_F^t$. The normal vector $\mathbf{N}$ and position vector $\mathbf{X}_V$ in the reference configuration are written as $\mathbf{n}$ and $\mathbf{x}_V$ when referring to the current configuration.

2.5.2 Approximation of the displacement

Both directional derivatives in Eqs. (15) and residuals in Eqs. (13) are approximated by lowest-order three-dimensional finite element formulations based on the scaled boundary

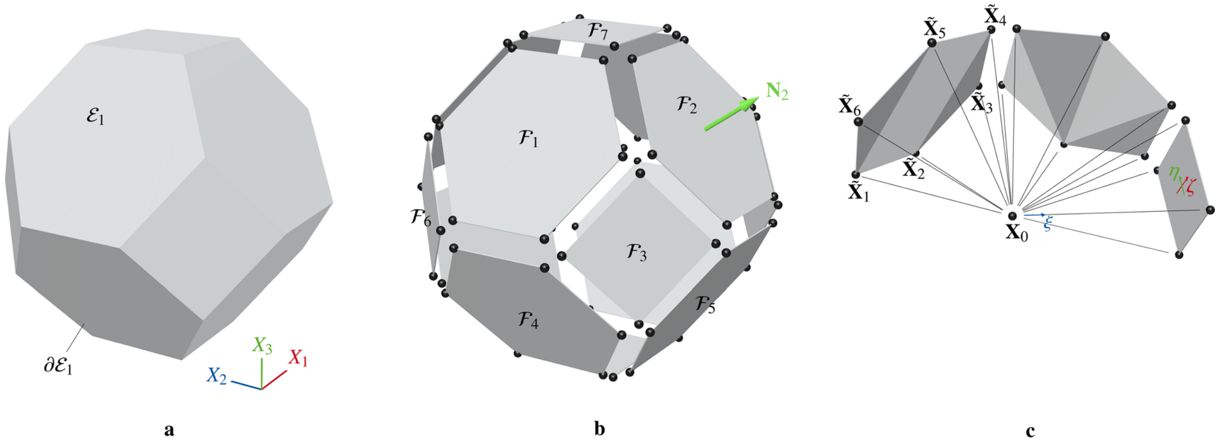

Fig. 2 **a** Bitruncated cubic honeycomb element with domain $\mathcal{E}_1$ and boundary $\partial\mathcal{E}_1$. **b** Boundary representation of the element with face domains $\mathcal{F}_1$ to $\mathcal{F}_{14}$ and normal vector on $\mathcal{F}_2$. **c** Scaling approach of three faces along the scaling direction ξ. Faces with $n_V > 4$ are partitioned in triangular or quadrilateral facets

parameterization [42]. The continuity requirement for the displacement field is fulfilled by choosing linear interpolation functions. To construct these, the polyhedron is split into a boundary surface and a scaling direction. Both are approximated individually in a 2D and 1D parameter space, respectively. The necessary three-dimensional interpolation functions are subsequently constructed by a tensor product rule.

Each face with domain $\mathcal{F}_F$ is partitioned into quadrilateral and triangular facets if $\mathcal{F}_F$ is spanned by more than 4 vertices ($n_V > 4$). Since all polyhedral elements considered in this article are strictly convex, partitioning is fast and straightforward. All faces F with $n_V = 3$ and $n_V = 4$ remain unchanged and are not partitioned. After all necessary subdivisions, the element boundary surface consists of triangular and quadrilateral faces only (Fig. 2c). Their corresponding two-dimensional interpolation functions in the parameter space of the boundary $(\eta, \zeta) \in [-1,\ 1] \times [-1,\ 1]$ are standard and can be found in many finite element textbooks [27]. Moreover, numerical integration is straightforward, since standard Gauss point locations and weights can be employed in these quadrilateral and triangular parameter spaces as well.

The approximation of the scaling direction requires the insertion of a local scaling center $\mathbf{X}_0$ in the interior of each polyhedron. Each scaling center possesses 3 degrees-of-freedom, which can be eliminated by static condensation on element level for most problems. For the sake of simplicity, its coordinates are chosen to be coincident with the centroid of each polyhedron. The scaling direction $\xi \in [0, 1]$ points from the scaling center to the boundary. The corresponding one-dimensional functions that interpolate the boundary displacements along the scaling direction read:

$$N_1(\xi) = 1 - \xi \quad \text{and} \quad N_2(\xi) = \xi. \tag{19}$$

The interpolation functions for a scaled boundary section are then constructed by a tensor product rule, leading to the functions

$$N_0(\xi) = 1 - \xi, \tag{20a}$$
$$N_1(\xi,\ \eta,\ \zeta) = \xi(1 - \eta - \zeta), \tag{20b}$$
$$N_2(\xi,\ \eta) = \xi\eta, \tag{20c}$$
$$N_3(\xi,\ \zeta) = \xi\zeta, \tag{20d}$$

for a tetrahedral section, and

$$N_0(\xi) = 1 - \xi, \tag{21a}$$
$$N_1(\xi,\ \eta,\ \zeta) = \frac{1}{4}\xi(1 - \eta)(1 - \zeta), \tag{21b}$$
$$N_2(\xi,\ \eta,\ \zeta) = \frac{1}{4}\xi(1 + \eta)(1 - \zeta), \tag{21c}$$
$$N_3(\xi,\ \eta,\ \zeta) = \frac{1}{4}\xi(1 + \eta)(1 + \zeta), \tag{21d}$$
$$N_4(\xi,\ \eta,\ \zeta) = \frac{1}{4}\xi(1 - \eta)(1 + \zeta), \tag{21e}$$

for a pyramidal section. The locations of the integration points are constructed in the same manner.

2.5.3 Approximation of the pressure

The linearized weak form of Eqs. (14) allows for a pressure jump across element boundaries. The lowest-order pressure is therefore defined by a constant function. It is noteworthy that the use of a single pressure degree-of-freedom per polyhedral element is the only possibility to alleviate volumetric locking in the lowest-order element. A section-wise discontinuous pressure leads, according to [8], to a strong enforcement of the incompressibility constraint of Eq. (6).

In the context of this work, it is shown later that a single pressure degree-of-freedom per polyhedron is a necessity to avoid spurious pressure modes.

2.5.4 Discrete linearized weak formulation

The interpolation functions of Eqs. (20) and (21) can be used to approximate the directional derivatives of Eqs. (15) in a standard manner. The discrete problem is written in a general discrete and linearized form as:

Find $(\mathbf{u}_h,\ p_h) \in \mathcal{U}_h\,(\Omega_h) \times \mathcal{P}_h\,(\Omega_h)$ such that

$$a(\delta\mathbf{u}_h,\ \Delta\mathbf{u}_h) + b(\delta\mathbf{u}_h,\ \Delta p_h) = f(\delta\mathbf{u}_h) - r_u(\delta\mathbf{u}_h) \quad \forall\ \delta\mathbf{u}_h \in \mathcal{U}_h\,(\Omega_h) \tag{22a}$$

$$b(\delta p_h,\ \Delta\mathbf{u}_h) - c(\delta p_h,\ \Delta p_h) = -r_p(\delta p_h) \quad \forall\ \delta p_h \in \mathcal{P}_h\,(\Omega_h) \tag{22b}$$

Here, $\mathcal{U}_h\,(\Omega_h)$ and $\mathcal{P}_h\,(\Omega_h)$ are the finite-dimensional subspaces corresponding to $\mathcal{H}^1_0\,(\Omega)$ and $\mathcal{L}^2\,(\Omega)$. The equivalent matrix equations to Eqs. (22) read:

$$\underbrace{\begin{bmatrix} \mathbf{K}_{\mathrm{uu}} & \mathbf{K}_{\mathrm{up}} \\ \mathbf{K}_{\mathrm{pu}} & -\mathbf{K}_{\mathrm{pp}} \end{bmatrix}}_{\mathbf{K}_T} \begin{bmatrix} \Delta\hat{\mathbf{u}} \\ \Delta\hat{\mathbf{p}} \end{bmatrix} = \begin{bmatrix} \mathbf{f} \\ \mathbf{0} \end{bmatrix} - \begin{bmatrix} \mathbf{r}_u \\ \mathbf{r}_p \end{bmatrix}, \tag{23}$$

where $\mathbf{K}_T$ is the tangent stiffness matrix, $\Delta\hat{\mathbf{u}}$ are the nodal incremental displacements and $\Delta\hat{\mathbf{p}}$ are incremental pressures.

2.6 Stability

The mixed system of equations in Eq. (23) must be solvable and stable. The coercivity condition and the Ladyzhenskaya–Babuška–Brezzi (LBB) condition [24–26], or inf-sup condition, provide the sufficient conditions to assess the stability of the mixed finite element formulation. Both conditions, herein evaluated for the tangent spaces due to linearization, are summarized in the following two paragraphs.

2.6.1 Coercivity on the kernel

One can find a unique displacement solution $\mathbf{u}_h$ if the bilinear form $a(\cdot,\ \cdot)$ is coercive in the nullspace of $b(\cdot,\ \cdot)$. This means that:

There exists a constant $\alpha > 0$ independent of the mesh size such that

$$a(\mathbf{u}_h,\ \mathbf{u}_h) > \alpha\ |\mathbf{u}_h|^2_{\mathcal{U}} \quad \forall\ \mathbf{u}_h \in \mathcal{K}_h, \tag{24}$$

where $\mathcal{K}_h$ is the discrete kernel of the mixed bilinear form:

$$\mathcal{K}_h = \left\{ \mathbf{u}_h \in \mathcal{U}_h \,\middle|\, b\,(\delta p_h,\ \mathbf{u}_h) = 0 \quad \forall\ \delta p_h \in \mathcal{P}_h \right\}. \tag{25}$$

For most classical finite element formulations in linear solid mechanics, coercivity is fulfilled. This may change when nonlinear problems with large deformations are considered. It is then possible that the tangent matrix $\mathbf{K}_{\mathrm{uu}}$ loses its positive-definiteness as soon as the load-deflection curve bifurcates. The reader is referred to References [43, 44] for a detailed discussion on the coercivity condition in mixed finite element analysis. In this article, we will not focus on this phenomenon and assume that Eq. (24) is fulfilled. The inf-sup condition then becomes the necessary criterion to guarantee a stable solution.

2.6.2 Inf-sup condition

The inf-sup condition, which poses the necessary condition for the bilinear operator $b(\cdot,\ \cdot)$ reads:

There exists a constant $\beta > 0$ independent of the mesh size such that

$$\inf_{\delta p_h \in \mathcal{P}_h(\Omega_h)} \ \sup_{\delta\mathbf{u}_h \in \mathcal{U}_h(\Omega_h)} \frac{b\,(\delta p_h,\ \delta\mathbf{u}_h)}{|\delta p_h|_{\mathcal{P}}\ |\delta\mathbf{u}_h|_{\mathcal{U}}} \geq \beta. \tag{26}$$

The condition depends on the chosen finite element approximation and mesh. In a discrete setting, Eq. (26) implies that $\mathbf{K}_{\mathrm{up}}$ is injective and no $\Delta\hat{\mathbf{p}} \neq \mathbf{0}$ satisfies

$$\mathbf{K}_{\mathrm{up}}\Delta\hat{\mathbf{p}} = \mathbf{0}. \tag{27}$$

It is important that this holds for any mesh density [45]. As soon as the nullspace of $\mathbf{K}_{\mathrm{up}}$ contains other vectors than the zero vector, the inf-sup condition fails. The nullspace vectors of $\mathbf{K}_{\mathrm{up}}$ are called spurious pressure modes. We now focus on these spurious pressure modes and aim to exclude them from the solution space of the pressure in order to fulfill the inf-sup condition.

3 Spurious pressure modes

3.1 Push-forward of the bilinear form

As mentioned in the previous section, a spurious pressure mode occurs if the nullspace of the bilinear form $b\,(\cdot,\ \cdot)$ consists of nontrivial pressure solutions. The only truly physical representation of such a pressure mode is a hydrostatic pressure mode, which is suppressed in a well-posed problem [46]. Any other pressure solution is considered to be spurious and may lead to severe pollution of the pressure field. In nonlinear analysis, the same considerations can be made and the inf-sup condition must be fulfilled considering the tangent spaces at any admissible displacement and pressure state.

Specializing on a lowest-order and three-dimensional mixed displacement-pressure formulation, we look for all possible pressure vectors in the nullspace of the discrete mixed bilinear form $b(\cdot,\ \cdot)$. The discontinuity of the pressure field allows us to pick an arbitrary vertex ($\star$) in the interior of the mesh and analyze the nullspace locally. In a somewhat different way compared to the two-dimensional derivation [39], but arriving at a similar expression, we discretize the mixed bilinear form at an arbitrary vertex ($\star$) for three-dimensional problems and employ a push-forward operation. We will assume that the vertex indicated by ($\star$) is connected to d_F faces F, to which we will assign the local face numbering $F = 1, 2, ..., d_F$. All vertices V belonging to any of these faces F are numbered locally as (1) – (2) – ... – ($n_V - 1$) – ($\star$). Since each element is built up by several faces, the vertex ($\star$) represents the intersection point of d_E elements. Examples fulfilling $d_E = 8$ and $d_E = 4$ are depicted in Fig. 3.

To analyze the nullspace of the mixed part of the stiffness matrix, see Eq.(27), we start with the directional derivative of Eq. (15b), which is:

$$b\left(\delta\mathbf{u},\ \Delta p\right) = \mathcal{D}_p G_u \cdot \Delta p = \int_{\Omega_h} \delta\mathbf{E} : \frac{\partial \hat{U}}{\partial \mathbf{E}}\ \Delta p\ \mathrm{d}V. \tag{28}$$

Expressing the derivative with respect to the Green-Lagrange strain tensor as

$$\frac{\partial \hat{U}}{\partial \mathbf{E}} = 2\,\frac{\partial\left(J-1\right)}{\partial \mathbf{C}} = J\mathbf{C}^{-1} = J\mathbf{F}^{-1}\mathbf{F}^{-\mathsf{T}}, \tag{29}$$

and substituting this into Eq. (28) yields:

$$b\left(\delta\mathbf{u},\ \Delta p\right) = \int_{\Omega_h} \delta\mathbf{E} : \mathbf{F}^{-1}\mathbf{F}^{-\mathsf{T}}\ \Delta p\ J\mathrm{d}V. \tag{30}$$

The pressure is now approximated by a constant interpolation function and the domain is reduced to a single element E with domain $\mathcal{E}_E$. Using $\mathrm{d}v = J\mathrm{d}V$, integration is carried out over the spatial domain $\mathcal{E}^t_E$ and Eq. (30) becomes

$$b_E\left(\delta\mathbf{u},\ \Delta p_E\right) = \int_{\mathcal{E}^t_E} \mathrm{Grad}\left(\delta\mathbf{u}\right) : \mathbf{F}^{-\mathsf{T}}\ \mathrm{d}v\ \Delta p_E, \tag{31}$$

Employing a push-forward operation on the displacement gradient yields:

$$b_E\left(\delta\mathbf{u},\ \Delta p_E\right) = \int_{\mathcal{E}^t_E} \mathrm{grad}\left(\delta\mathbf{u}\right)\mathbf{F} : \mathbf{F}^{-\mathsf{T}}\ \mathrm{d}v\ \Delta p_E \tag{32}$$

$$= \int_{\mathcal{E}^t_E} \mathrm{div}\left(\delta\mathbf{u}\right)\ \mathrm{d}v\ \Delta p_E. \tag{33}$$

Finally, the integral can be transferred to the deformed element boundary using the divergence theorem:

$$b_E\left(\delta\mathbf{u},\ \Delta p_E\right) = \int_{\partial\mathcal{E}^t_E} \delta\mathbf{u}^{\mathsf{T}}\ \mathbf{n}\ \mathrm{d}a\ \Delta p_E. \tag{34}$$

Consequently, the normal vector $\mathbf{n} \in \mathbb{R}^3$ and the differential area $\mathrm{d}a$ refer to the current configuration. A face F of the element E, which is connected to the vertex ($\star$), is considered. The virtual displacement vector $\delta\mathbf{u}$ on this face can be approximated as:

$$\delta\mathbf{u}_h = \begin{bmatrix}\mathbf{H}_1 & \mathbf{H}_2 & \dots & \mathbf{H}_{n_V-1} & \mathbf{H}_\star\end{bmatrix} \begin{bmatrix}\delta\mathbf{u}_1\\ \delta\mathbf{u}_2\\ \vdots\\ \delta\mathbf{u}_{n_V-1}\\ \delta\mathbf{u}_\star\end{bmatrix}, \tag{35}$$

with

$$\mathbf{H}_V = H_V(\eta, \zeta)\mathbf{I}_{3\times 3} \tag{36}$$

Here, $\delta\mathbf{u}_V \in \mathbb{R}^{3\times 1}$ define the nodal virtual displacement vectors of all nodes $V = 1, 2, ..., n_V$ connected to the considered face. The functions $H_V(\eta, \zeta)$ represent interpolation functions on the boundary. Evaluating Eq. (34) for the face F, considering the approximation of Eq. (35), one obtains:

$$b_F\left(\delta\mathbf{u}_h,\ \Delta p_E\right) = \int_{\mathcal{F}^t_F} \delta\mathbf{u}_h^{\mathsf{T}}\ \mathbf{n}_F\ \mathrm{d}a_F\ \Delta p_E \tag{37a}$$

$$= \sum_{V=1}^{n_V-1} \delta\mathbf{u}_V^{\mathsf{T}} \int_{\Box} \mathbf{H}_V^{\mathsf{T}}\ \det\bar{\mathbf{j}}\ \mathrm{d}\Box\ \mathbf{n}_F\ \Delta p_E \tag{37b}$$

$$+\ \delta\mathbf{u}_\star^{\mathsf{T}} \int_{\Box} \mathbf{H}_\star^{\mathsf{T}}\ \det\bar{\mathbf{j}}\ \mathrm{d}\Box\ \mathbf{n}_F\ \Delta p_E \tag{37c}$$

$$= \underbrace{\sum_{V=1}^{n_V-1} \delta\mathbf{u}_V^{\mathsf{T}}\ \alpha_V\ \mathbf{n}_F\ \Delta p_E}_{b_V} + \underbrace{\delta\mathbf{u}_\star^{\mathsf{T}}\ \alpha_\star\ \mathbf{n}_F\ \Delta p_E}_{b_\star}, \tag{37d}$$

where $\int_\Box (\cdot)\ \mathrm{d}\Box = \int_{-1}^{1}\int_{-1}^{1} (\cdot)\ \mathrm{d}\zeta\mathrm{d}\eta$. The differential area $\mathrm{d}a$ is mapped to the parameter space using the determinant of the spatial Jacobian matrix on the element boundary. Due to the fact that the interpolation functions $H_V(\eta, \zeta)$ and the determinant $\det\bar{\mathbf{j}}$ are strictly positive on any convex face, we can guarantee that

$$\alpha_V = \int_\Box \mathbf{H}_V^{\mathsf{T}}\ \det\bar{\mathbf{j}}\ \mathrm{d}\Box > 0 \quad \forall\ V. \tag{38}$$

The term $b_\star$ in Eq. (37d) couples the virtual displacements of vertex ($\star$) to a corresponding constant pressure. The vector

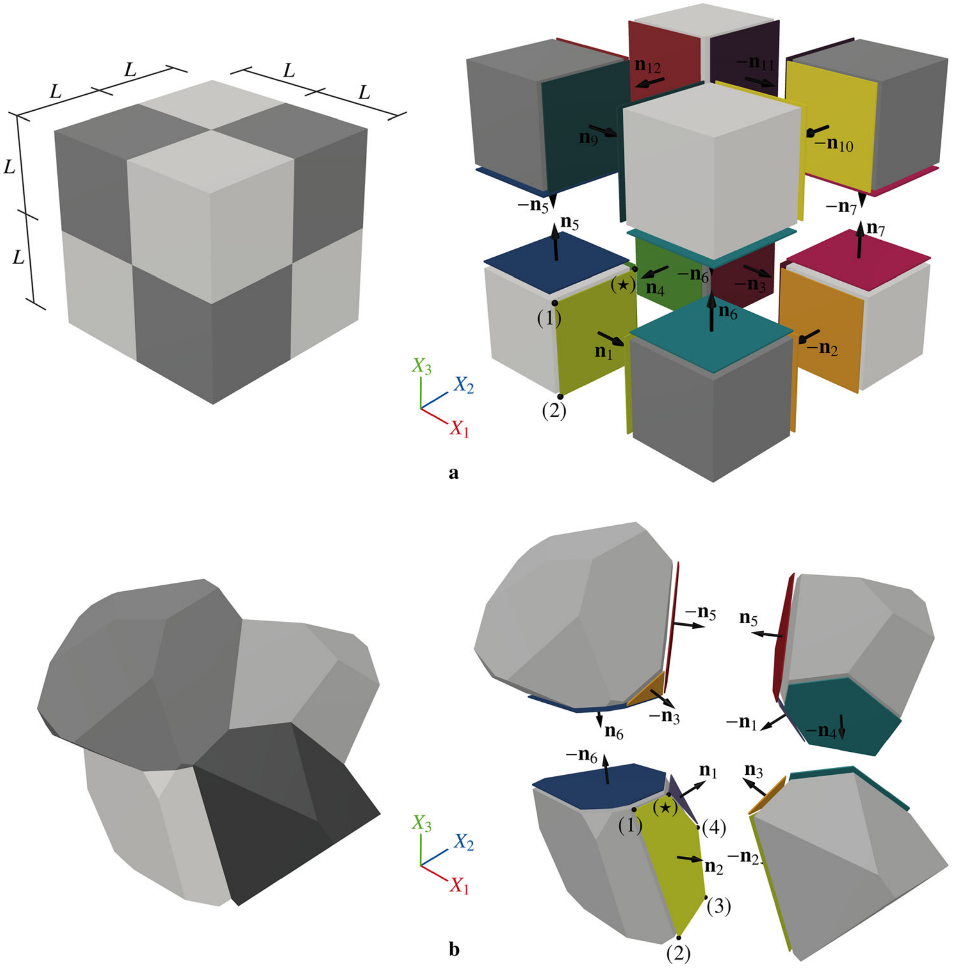

Fig. 3 **a** Patch of eight hexahedral elements intersecting in vertex ($\star$). **b** Patch of four polyhedral elements intersecting in vertex ($\star$)

$\alpha_\star \mathbf{n}_F$ contains the three coupled tangent stiffness entries of these degrees-of-freedom.

In the interior of a finite element mesh, an arbitrary number of elements d_E intersect in each vertex ($\star$). This means that the stiffness entries included in $b_\star$ must be assembled. Since the pressure is discontinuous, all pressures in neighboring elements are uncoupled. It is thus sufficient to consider the local vertex ($\star$) and investigate whether or not a spurious pressure mode can develop in the elements around this node. Considering the assembly of the discrete bilinear operators $b_\star$ into $B_\star$, a system of equations is obtained, which reads

$$B_\star\,(\delta \mathbf{u}_\star,\ \Delta p_E) = \delta \mathbf{u}_\star^\top \underbrace{\begin{bmatrix} \mathbf{m}_1 & \mathbf{m}_2 & \dots & \mathbf{m}_{d_E} \end{bmatrix}}_{\mathbf{K}^\star_{\mathrm{up}}} \underbrace{\begin{bmatrix} \Delta p_1 \\ \Delta p_2 \\ \vdots \\ \Delta p_{d_E} \end{bmatrix}}_{\Delta \mathbf{p}^\star}, \tag{39}$$

where $\mathbf{K}^\star_{\mathrm{up}} \in \mathbb{R}^{3\times d_E}$ is the local stiffness matrix coupling the three displacements at the vertex ($\star$) with d_E pressure increments in the adjacent elements. Recalling the definition of a spurious pressure mode, we now seek for all pressure vectors $\Delta \mathbf{p}^\star$ in the nullspace of $\mathbf{K}^\star_{\mathrm{up}}$. Assuming $\operatorname{rank}(\mathbf{K}^\star_{\mathrm{up}}) = 3$, it follows from the rank-nullity theorem that

$$\operatorname{nullity}(\mathbf{K}^\star_{\mathrm{up}}) = d_E - 3. \tag{40}$$

There are thus $d_E - 3$ basis vectors in the nullspace of $\mathbf{K}^\star_{\mathrm{up}}$. The suppression of these nullspace vectors for any level of mesh refinement results in inf-sup stability.

3.2 Spurious pressure modes in a hexahedral mesh

For the sake of completeness, we illustrate that the H1/P0 element is inf-sup unstable and prone to display spurious pressure modes. We therefore assemble Eq. (39) at an arbitrary interior vertex ($\star$) for $d_E = 8$ elements with trilinear displacements and constant pressure (H1/P0). For the sake of simplicity, it is assumed that the current configuration contains undistorted hexahedral finite elements with edge length L.

Considering Eq. (39) for the set of hexahedral elements with the face and normal vector numbering as in Fig. 3a, we obtain

$$B_\star(\delta\mathbf{u}_\star,\ \Delta p_E) = \delta\mathbf{u}_\star^\mathsf{T} \underbrace{\left[\mathbf{m}_1\ \ \mathbf{m}_2\ \ \ldots\ \ \mathbf{m}_8\right]}_{\mathbf{K}_{\text{up}}^\star} \underbrace{\begin{bmatrix}\Delta p_1\\ \Delta p_2\\ \vdots\\ \Delta p_8\end{bmatrix}}_{\Delta\mathbf{p}^\star}, \tag{41}$$

where the vectors $\mathbf{m}_i$ are expressed for this specific mesh layout as

$$\mathbf{m}_1 = \alpha_{\star,1}\mathbf{n}_1 + \alpha_{\star,5}\mathbf{n}_5 - \alpha_{\star,4}\mathbf{n}_4, \tag{42a}$$
$$\mathbf{m}_2 = \alpha_{\star,2}\mathbf{n}_2 + \alpha_{\star,6}\mathbf{n}_6 - \alpha_{\star,1}\mathbf{n}_1, \tag{42b}$$
$$\mathbf{m}_3 = \alpha_{\star,3}\mathbf{n}_3 + \alpha_{\star,7}\mathbf{n}_7 - \alpha_{\star,2}\mathbf{n}_2, \tag{42c}$$
$$\mathbf{m}_4 = \alpha_{\star,4}\mathbf{n}_4 + \alpha_{\star,8}\mathbf{n}_8 - \alpha_{\star,3}\mathbf{n}_3, \tag{42d}$$
$$\mathbf{m}_5 = \alpha_{\star,9}\mathbf{n}_9 - \alpha_{\star,5}\mathbf{n}_5 - \alpha_{\star,12}\mathbf{n}_{12}, \tag{42e}$$
$$\mathbf{m}_6 = \alpha_{\star,10}\mathbf{n}_{10} - \alpha_{\star,9}\mathbf{n}_9 - \alpha_{\star,6}\mathbf{n}_6, \tag{42f}$$
$$\mathbf{m}_7 = \alpha_{\star,11}\mathbf{n}_{11} - \alpha_{\star,10}\mathbf{n}_{10} - \alpha_{\star,7}\mathbf{n}_7, \tag{42g}$$
$$\mathbf{m}_8 = \alpha_{\star,12}\mathbf{n}_{12} - \alpha_{\star,11}\mathbf{n}_{11} - \alpha_{\star,8}\mathbf{n}_8. \tag{42h}$$

Due to our assumption regarding the edge length L, all scaling factors are

$$\alpha_{\star,F} = \int_\square \mathbf{H}_V^\mathsf{T} \det\bar{\mathbf{j}}\ \mathrm{d}\square = \frac{L^2}{4} \tag{43}$$

and Eq. (41) becomes

$$\frac{L^2}{4}\begin{bmatrix}1 & -1 & -1 & 1 & 1 & -1 & -1 & 1\\ 1 & 1 & -1 & -1 & 1 & 1 & -1 & -1\\ 1 & 1 & 1 & 1 & -1 & -1 & -1 & -1\end{bmatrix}\begin{bmatrix}\Delta p_1\\ \Delta p_2\\ \Delta p_3\\ \Delta p_4\\ \Delta p_5\\ \Delta p_6\\ \Delta p_7\\ \Delta p_8\end{bmatrix} = \mathbf{0} \tag{44}$$

By looking at $\mathbf{K}_{\text{up}}^\star$, we see that

$$\operatorname{rank}(\mathbf{K}_{\text{up}}^\star) = 3 \tag{45}$$

and there are thus five basis vectors in its nullspace. The nullspace method (see e.g. [47]) is used to find these vectors $\Delta\mathbf{p}_s^\star$, where the subscript s denotes that these vectors are spurious pressure modes. The matrix $\mathbf{K}_{\text{up}}^\star$ is regular, allowing for a LQ-factorization which is of the form

$$\mathbf{K}_{\text{up}}^\star = \left[\mathbf{L}\ \mathbf{0}\right]\begin{bmatrix}\tilde{\mathbf{Q}}\\ \hat{\mathbf{Q}}\end{bmatrix}. \tag{46}$$

Here, $\mathbf{L} \in \mathbb{R}^{3\times 3}$ is a lower triangular matrix, $\tilde{\mathbf{Q}} \in \mathbb{R}^{3\times 8}$ and $\hat{\mathbf{Q}} \in \mathbb{R}^{5\times 8}$. The vectors in $\hat{\mathbf{Q}}$ span the null basis of $\mathbf{K}_{\text{up}}^\star$. All solutions to Eq. (44) can now be calculated as

$$\Delta\mathbf{p}_s^\star = \hat{\mathbf{Q}}^\mathsf{T}\,\mathbf{z} \qquad \forall\,\mathbf{z} \in \mathbb{R}^{5\times 1}, \tag{47}$$

or for this specific problem:

$$\mathbf{Q}^\mathsf{T} = \frac{L^2}{4}\begin{bmatrix}-0.3536 & -0.1934 & +0.3536 & +0.5801 & +0.0332\\ +0.3536 & +0.0332 & -0.3536 & +0.1934 & +0.5801\\ -0.3536 & +0.5801 & +0.3536 & -0.0332 & +0.1934\\ +0.7230 & +0.0923 & +0.2770 & +0.0923 & -0.0923\\ +0.0923 & +0.7648 & -0.0923 & +0.1515 & +0.0087\\ +0.2770 & -0.0923 & +0.7230 & -0.0923 & +0.0923\\ +0.0923 & -0.0087 & -0.0923 & +0.7648 & -0.1515\\ -0.0923 & -0.1515 & +0.0923 & +0.0087 & +0.7648\end{bmatrix} \tag{48}$$

All nullspace vectors are thus linear combinations of the columns of $\mathbf{Q}^\mathsf{T}$. The well-known pure checkerboard mode, which is of the form

$$\Delta\mathbf{p}_s^\star = \left[+1\ \ -1\ \ +1\ \ -1\ \ -1\ \ +1\ \ -1\ \ +1\right]^\mathsf{T}, \tag{49}$$

is part of the nullspace of $\mathbf{K}_{\text{up}}^\star$ and corresponds to

$$\mathbf{z} = \left[-1.6882\ \ -1.0646\ \ +1.6882\ \ -1.0646\ \ +0.1827\right]^\mathsf{T}. \tag{50}$$

The hydrostatic pressure mode is part of the nullspace and is determined by substituting

$$\mathbf{z} = \left[+0.1827\ \ +1.3764\ \ +1.8173\ \ +1.3764\ \ +0.9354\right]^\mathsf{T} \tag{51}$$

into Eq. (47), from which

$$\Delta\mathbf{p}_s^\star = \left[+1\ \ +1\ \ +1\ \ +1\ \ +1\ \ +1\ \ +1\ \ +1\right]^\mathsf{T}, \tag{52}$$

is obtained. The occurrence of such pressure modes in the finite element solution is dependent on the imposed boundary conditions. Only in specially constructed problems, spurious modes are visible on the complete domain (see e.g. [27]). More occasionally, spurious pressure modes occur locally in constrained parts of the domain (see e.g. [11, 19, 39]). Due to the fact that in 3D, the spurious modes are linear combinations of multiple nullspace vectors, the application of smoothing and filtering techniques on the unstable pressure field is challenging.

Moreover, the methodology to identify spurious pressure modes is not limited to regular meshes with undistorted hexahedral elements, but can be used for arbitrary quadrilaterals as well. In these cases, the outward unit normal vectors $\mathbf{n}_F$ of an element E are not necessarily orthonormal and the scaling factors $\alpha_{\star,F}$ are no longer constant. Still, one can show that spurious pressure modes can develop on such meshes. A numerical example to demonstrate the spurious pattern on a distorted two-dimensional quadrilateral mesh can be found in [39].

3.3 Reduction of the number of intersecting elements

It has now become clear that the existence of spurious pressure modes is dependent on the mesh and the interpolation orders of both displacement and pressure. Keeping the interpolation orders as low as possible, we aim to stabilize the lowest-order element by changing the meshing strategy. To do so, the nullity of $\mathbf{K}^\star_{\mathrm{up}}$ must be minimized, so that the hydrostatic pressure mode $\Delta\mathbf{p}^\star_s$ is the only nullspace basis vector of $\mathbf{K}^\star_{\mathrm{up}}$. By reducing the number of elements coincident to each vertex, there are fewer columns in $\mathbf{K}^\star_{\mathrm{up}}$, leading to a decrease in spurious pressure modes due to the rank-nullity theorem.

Considering that elements with at least 4 vertices (tetrahedra) are needed to span a 3D space, one can use the concept of duality to verify that $d_E \geq 4$ in 3D [48]. This means that there are at least 4 elements connected to each vertex in a 3D mesh. Similar to the derivation of Sec. 3.2, we therefore derive $\mathbf{K}^\star_{\mathrm{up}}$ for a patch of elements fulfilling $d_E = 4$ to make sure that there will be only one nullspace basis vector. It will be shown later in Sec. 3.4 that the element geometries corresponding to meshes fulfilling $d_E = 4$ will be polyhedral and require polyhedral finite element formulations. Note that the use of the polyhedral finite element formulation of Sec. 2.5 does not alter the derivation presented before, since the interpolation functions on the boundary remain linear.

Without restricting the element geometry, the assembled discrete bilinear operator of Eq. (39) for $d_E = 4$ now reads

$$B_\star\left(\delta\mathbf{u}_\star,\ \Delta p_E\right) = \delta\mathbf{u}_\star^{\mathsf{T}} \underbrace{\begin{bmatrix}\mathbf{m}_1 & \mathbf{m}_2 & \mathbf{m}_3 & \mathbf{m}_4\end{bmatrix}}_{\mathbf{K}^\star_{\mathrm{up}}} \underbrace{\begin{bmatrix}\Delta p_1\\ \Delta p_2\\ \Delta p_3\\ \Delta p_4\end{bmatrix}}_{\Delta\mathbf{p}^\star}, \tag{53}$$

with

$$\mathbf{m}_1 = \alpha_{\star,1}\mathbf{n}_1 + \alpha_{\star,2}\mathbf{n}_2 - \alpha_{\star,6}\mathbf{n}_6, \tag{54a}$$

$$\mathbf{m}_2 = \alpha_{\star,3}\mathbf{n}_3 - \alpha_{\star,2}\mathbf{n}_2 + \alpha_{\star,4}\mathbf{n}_4, \tag{54b}$$

$$\mathbf{m}_3 = \alpha_{\star,5}\mathbf{n}_5 - \alpha_{\star,1}\mathbf{n}_1 - \alpha_{\star,4}\mathbf{n}_4, \tag{54c}$$

$$\mathbf{m}_4 = \alpha_{\star,6}\mathbf{n}_6 - \alpha_{\star,3}\mathbf{n}_3 - \alpha_{\star,5}\mathbf{n}_5, \tag{54d}$$

according to the assumed face numbering of Fig. 3b. We assume that all normal vectors corresponding to the same finite element are linearly independent (i.e. no two coincident faces are coplanar). The rank-nullity theorem states that there is only one null basis vector corresponding to the matrix $\mathbf{K}^\star_{\mathrm{up}}$. The only pressure vector allowed to be a nullspace vector of $\mathbf{K}^\star_{\mathrm{up}}$ is the hydrostatic pressure. As long as the system is well-posed, this mode will not occur in the solution and the overall pressure solution is well-posed [46]. To determine the nullspace of $\mathbf{K}^\star_{\mathrm{up}}$, the matrix is brought into reduced row echelon form (RREF). After several mathematical manipulations, we obtain

$$\mathbf{R} = \mathrm{RREF}\left(\mathbf{K}^\star_{\mathrm{up}}\right) = \begin{bmatrix}1 & 0 & 0 & R_{14}\\ 0 & 1 & 0 & R_{24}\\ 0 & 0 & 1 & R_{34}\end{bmatrix} \tag{55}$$

where R_{14}, R_{24} and R_{34} can be evaluated as

$$R_{14} = \frac{(\mathbf{m}_2 \times \mathbf{m}_3)\cdot\mathbf{m}_4}{(\mathbf{m}_1 \times \mathbf{m}_2)\cdot\mathbf{m}_3}, \tag{56a}$$

$$R_{24} = -\frac{(\mathbf{m}_1 \times \mathbf{m}_3)\cdot\mathbf{m}_4}{(\mathbf{m}_1 \times \mathbf{m}_2)\cdot\mathbf{m}_3}, \tag{56b}$$

$$R_{34} = \frac{(\mathbf{m}_1 \times \mathbf{m}_2)\cdot\mathbf{m}_4}{(\mathbf{m}_1 \times \mathbf{m}_2)\cdot\mathbf{m}_3}. \tag{56c}$$

After substituting Eqs. (54) and evaluating all expressions, it follows that $R_{14} = R_{24} = R_{34} = -1$. Setting $\Delta p_4 = \Delta\check{p}$, the only nullspace vector of $\mathbf{K}^\star_{\mathrm{up}}$ is thus equal to

$$\Delta\mathbf{p}^\star_s = \begin{bmatrix}\Delta\check{p} & \Delta\check{p} & \Delta\check{p} & \Delta\check{p}\end{bmatrix}^{\mathsf{T}}, \tag{57}$$

which corresponds to the hydrostatic pressure mode. Note that the case in which

$$(\mathbf{m}_1 \times \mathbf{m}_2)\cdot\mathbf{m}_3 = 0 \tag{58}$$

leads to a degenerate mesh configuration, and is excluded.

3.4 Voronoi meshes

It is now clear that no more than four finite elements must coincide in a finite element vertex to ensure that all possible spurious pressure modes are suppressed. Meshes that fulfill this property can be constructed using Voronoi tessellations. From now on, we will use the terms *element* instead of the usual *region* and *mesh* instead of *tessellation* to retain the usual FEM terminology.

To construct the Voronoi mesh, a boundary description of the domain Ω and a set of sites $\mathcal{S}$ are needed. A site can be located inside, on, or outside of the boundary. The construction of a finite element E corresponding to its site $\mathbf{s}_E$ follows from [48]:

$$\begin{aligned}\mathcal{E}_E\left(\mathbf{s}_E\right) = \{\mathbf{x} \in \mathbb{R}^3 : &\|\mathbf{x} - \mathbf{s}_E\|_{\mathcal{L}^2}\\ &\leq \|\mathbf{x} - \mathbf{s}_I\|_{\mathcal{L}^2}\ \forall\ E \neq I\},\end{aligned} \tag{59}$$

which states that all points in the element domain $\mathcal{E}_E$ are closer to the site $\mathbf{s}_E$ than to any other site. Correspondingly, a face F of a finite element E is defined as

$$\begin{aligned}\mathcal{F}_F\left(\mathbf{s}_E\right) = \{\mathbf{x} \in \mathbb{R}^3 : &\|\mathbf{x} - \mathbf{s}_E\|_{\mathcal{L}^2}\\ &= \|\mathbf{x} - \mathbf{s}_I\|_{\mathcal{L}^2}\ \forall\ E \neq I\}.\end{aligned} \tag{60}$$

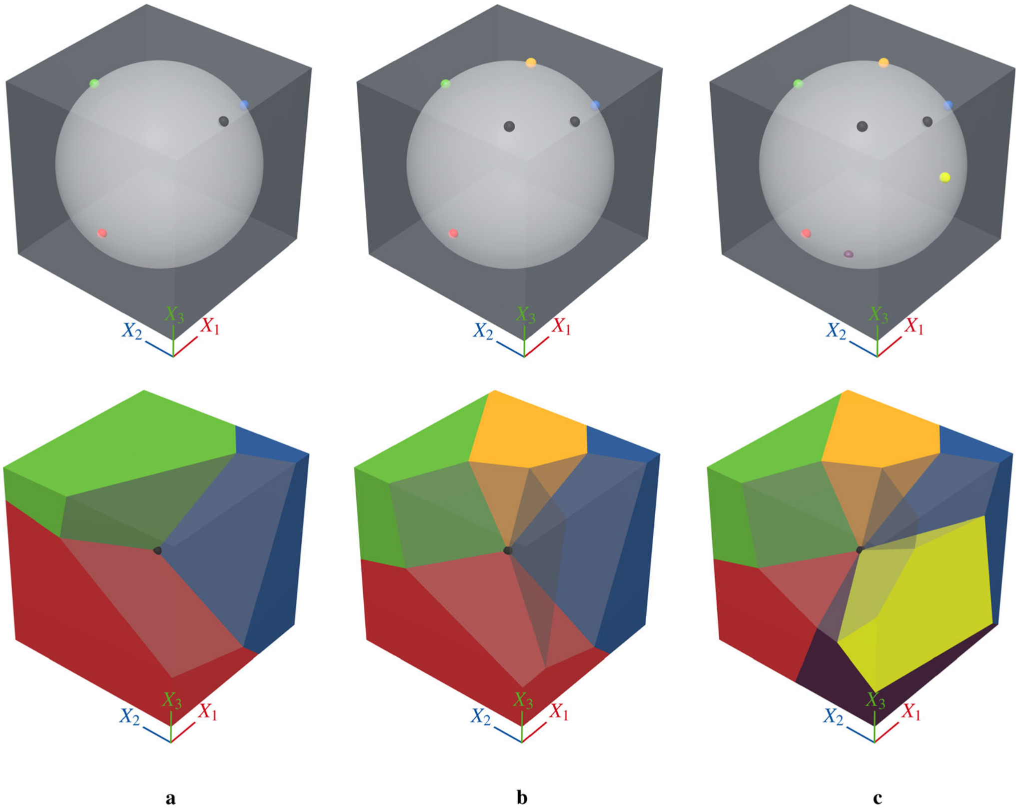

a

b

c

Fig. 4 Voronoi discretizations of a cube. **a** Four cospherical sites, $d_E = 4$, non-degenerate. **b** Six cospherical sites, $d_E = 6$, degenerate. **c** Eight cospherical sites, $d_E = 8$, degenerate

and is the bisector of two sites. A vertex is the intersection point of multiple faces and elements. Since all faces are equidistant to their two corresponding sites, a vertex is equidistant to several sites as well. This means that each finite element vertex is located at the center of a sphere passing through these sites. The number of sites on the sphere defines the number of elements that intersect in the vertex [48]. Three exemplary site layouts are shown in Fig. 4. One can recognize that the vertex-to-element ratio is equal to d_E if exactly d_E sites lie on the same sphere.

We can now utilize this property of a Voronoi discretization to construct a finite element mesh that suppresses spurious modes and fulfills $d_E \leq 4$. That is, if one can guarantee *a priori* that no more than four sites are cospherical, there are at most four elements coincident to each node and $d_E \leq 4$. Voronoi meshes that fulfill this property are referred to as non-degenerate. The generation of Voronoi sites that fulfill this property is simple. By selecting a random distribution of sites, the Voronoi mesh is always non-degenerate. This can be guaranteed since there exists no sphere that passes through more than four randomly sampled sites. A drawback of this method is, that the constructed meshes become highly irregular and distorted, and may therefore lead to slow convergence within the framework of the FEM. Relaxation algorithms (e.g. Lloyd relaxation [49]) can be employed to regularize the Voronoi mesh and transform the mesh into a centroidal Voronoi mesh. These meshes are nonsymmetric in general and may still contain irregularities between the elements. This can be overcome by manually placing the sites in a predefined layout. The approach can yield symmetric meshes (if the set of sites is symmetric), however, one needs to define all sites with care, since a degenerate mesh is easily generated. These degeneracies mostly occur when 2D meshes are extruded along a third dimension. Another example of such a mesh is a hexahedral discretization, in which $d_E = 8$.

3.5 Applicability to other formulations

The push-forward operation on the mixed bilinear form in Sec. 3.1 includes the transformation of the integral from the element volume to the element boundary. This indicates that solely the displacement approximation on the element boundary combined with a constant element-wise pressure is needed to prove inf-sup stability. It is therefore expected that the same considerations carry over to other polyhedral finite element formulations, especially the Virtual Element Method (VEM) [50]. Since in the VEM, only the boundary

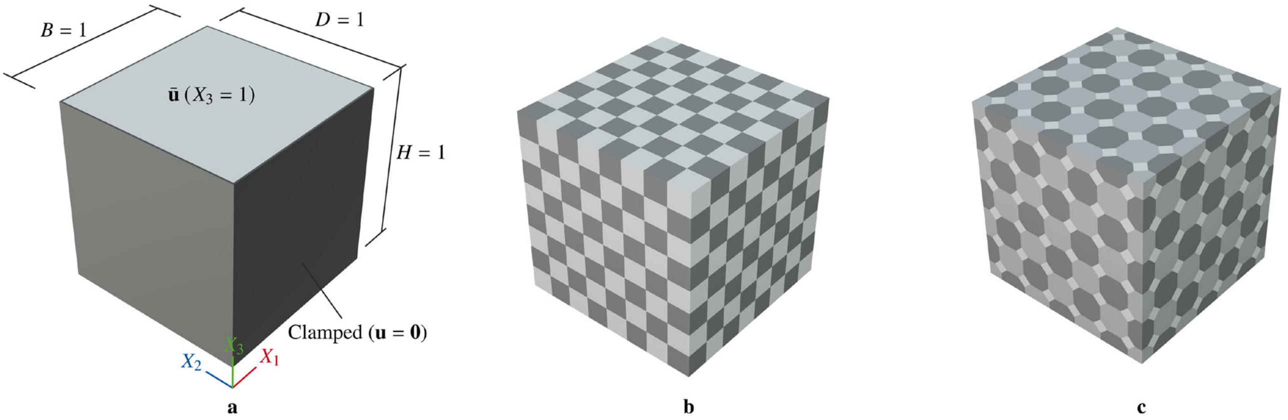

Fig. 5 Lid-driven cavity. **a** Dimensions and boundary conditions. **b** Hexahedral mesh with $N = 8$ (512 elements). **c** Bitruncated cubic honeycomb mesh with $M = 6$ (559 elements)

is known to be linearly interpolated on the lowest-order element, it is expected that virtual elements that incorporate a constant Lagrange multiplier can be stabilized using Voronoi meshes. The applicability of our approach could be validated using the formulations in [10] for problems in finite elasticity or [51] for topology optimization.

Moreover, spurious pressure modes are reported on mixed serendipity virtual elements with quadratic interpolation functions and a constant pressure (VEMS-D), see [52]. It is therefore certainly or interest to verify the inf-sup condition using the proposed method for quadratic interpolation functions and constant pressures as well.

4 Numerical examples

4.1 Lid-driven cavity

A three-dimensional unit cube $\Omega = [0, 1]^3 \subset \mathbb{R}^3$ is considered. The body is described by a linear elastic nearly-incompressible material law with Young's modulus $E = 100$ and Poisson's ratio $\nu = 0.4999$. All units are chosen consistently and are therefore omitted. Homogeneous Dirichlet boundary conditions are applied on the X_1- and X_2-components of $\partial\Omega \setminus \{\mathbf{X} \in \Omega \mid X_3 = 1\}$. Additionally, all X_3-components of the displacement are fixed on the boundary $\partial\Omega$. Nonhomogeneous Dirichlet conditions are applied on the X_1- and X_2-components on $\{\mathbf{X} \in \Omega \mid X_3 = 1\}$ according to the function

$$\begin{bmatrix}\bar{u}_1\\ \bar{u}_2\end{bmatrix} = \sin(\pi X_1)\sin(\pi X_2)\begin{bmatrix}0.1\\ 0.1\end{bmatrix}. \tag{61}$$

The domain and the corresponding boundary conditions are shown in Fig. 5a. The symmetry of the domain and the Dirichlet conditions motivate the use of a symmetric domain discretization. A Voronoi meshing algorithm is therefore used to generate two types of meshes. First, a regular cubical grid of Voronoi sites is defined and referred to as the set $\mathcal{S}_{\text{HEX}}$, which is

$$\begin{aligned}\mathcal{S}_{\text{HEX}} = &\left\{\frac{1}{2N}, \frac{3}{2N}, \dots, \frac{2N-1}{2N}\right\}\\ &\times\left\{\frac{1}{2N}, \frac{3}{2N}, \dots, \frac{2N-1}{2N}\right\}\\ &\times\left\{\frac{1}{2N}, \frac{3}{2N}, \dots, \frac{2N-1}{2N}\right\},\end{aligned} \tag{62}$$

with $N \in \mathbb{N}$. It can easily be shown that the set $\mathcal{S}_{\text{HEX}}$ is degenerate and eight sites are cospherical. Consequently, this layout leads to a mesh containing $n_E = N^3$ undistorted hexahedral elements. Additionally, a set $\mathcal{S}_{\text{HCB}}$ of Voronoi sites is constructed by the union of two subsets $\mathcal{S}^1_{\text{HCB}}$ and $\mathcal{S}^2_{\text{HCB}}$ as

$$\mathcal{S}_{\text{HCB}} = \mathcal{S}^1_{\text{HCB}} \cup \mathcal{S}^2_{\text{HCB}}, \tag{63}$$

where

$$\begin{aligned}\mathcal{S}^1_{\text{HCB}} = &\left\{0, \frac{1}{M}, ..., 1\right\} \times \left\{0, \frac{1}{M}, \dots, 1\right\}\\ &\times\left\{0, \frac{1}{M}, \dots, 1\right\},\end{aligned} \tag{64}$$

and

$$\begin{aligned}\mathcal{S}^2_{\text{HCB}} = &\left\{\frac{1}{2M}, \frac{3}{2M}, \dots, \frac{2M-1}{2M}\right\}\\ &\times\left\{\frac{1}{2M}, \frac{3}{2M}, \dots, \frac{2M-1}{2M}\right\}\\ &\times\left\{\frac{1}{2M}, \frac{3}{2M}, \dots, \frac{2M-1}{2M}\right\},\end{aligned} \tag{65}$$

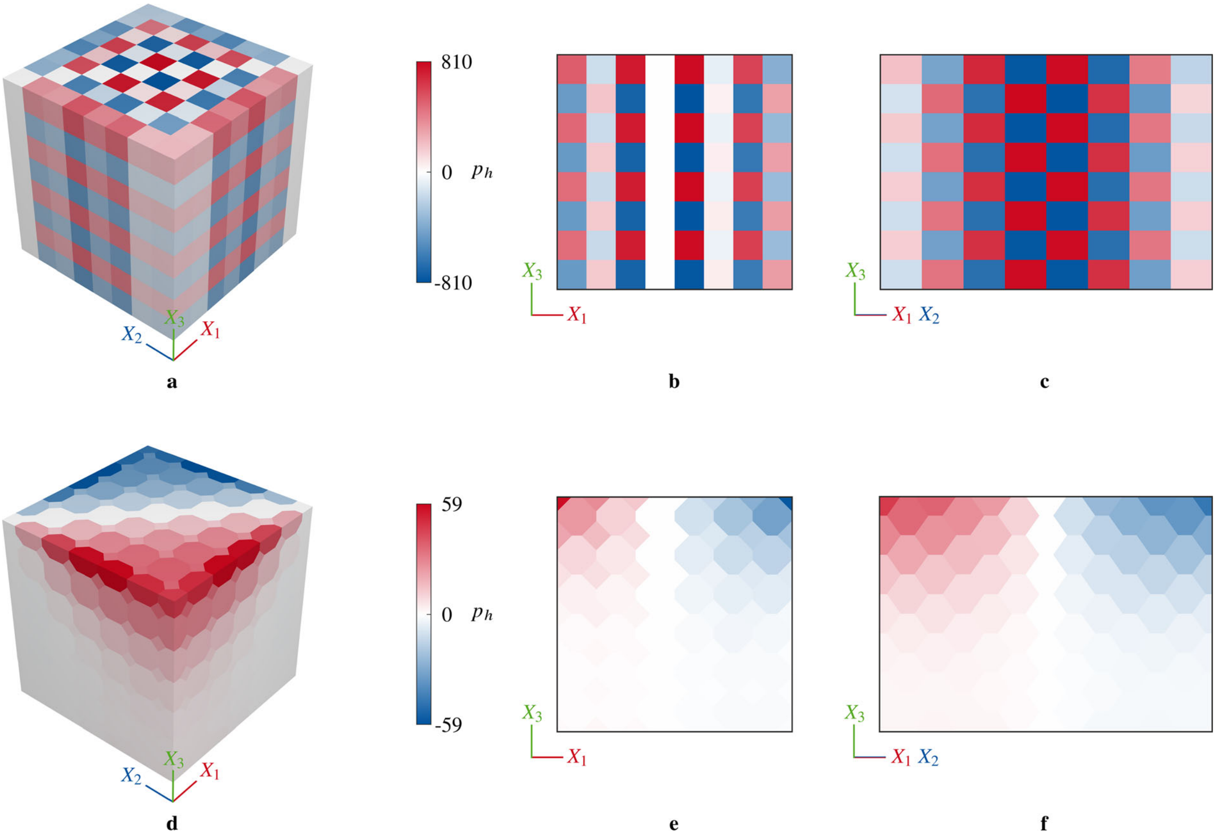

Fig. 6 Lid-driven cavity. **a** Pressures evaluated on the mesh based on $\mathcal{S}_{\text{HEX}}$ in the domain Ω. **b** Pressures ($\mathcal{S}_{\text{HEX}}$) on the hyperplane $\mathcal{P}_1$. **c** Pressures ($\mathcal{S}_{\text{HEX}}$) on the hyperplane $\mathcal{P}_2$. **d** Pressures evaluated on the mesh based on $\mathcal{S}_{\text{HCB}}$ in the domain Ω. **e** Pressures ($\mathcal{S}_{\text{HCB}}$) on the hyperplane $\mathcal{P}_1$. **f** Pressures ($\mathcal{S}_{\text{HCB}}$) on the hyperplane $\mathcal{P}_2$

with $M \in \mathbb{N}$, leading to a total of $n_E = M^3 + (M+1)^3$ elements. It can be shown that no more than four sites in $\mathcal{S}_{\text{HCB}}$ are cospherical, indicating that this arrangement of seed points leads to a non-degenerate Voronoi mesh; in this case a bitruncated cubic honeycomb (HCB) pattern. The non-degeneracy of the mesh indicates that a maximum of four elements per vertex are guaranteed and the solution should be free of spurious pressure modes.

The lid-driven cavity problem is solved on the two meshes based on the sets $\mathcal{S}_{\text{HEX}}$ with $N = 8$ (Fig. 5b) and $\mathcal{S}_{\text{HCB}}$ with $M = 6$ (Fig. 5c). The mesh based on $\mathcal{S}_{\text{HEX}}$ is approximated by the H1/P0 element, while the mesh corresponding to the set $\mathcal{S}_{\text{HCB}}$ is discretized by the mixed polyhedral finite element formulation presented in Sec. 2.

The pressure distribution of the problem for both mesh configurations is depicted in Fig. 6. The interior of the cube is visualized by slicing the domain using two hyperplanes $\mathcal{P}_1 = \{\mathbf{X} \in \Omega \mid X_2 = \frac{9}{16}\}$ and $\mathcal{P}_2 = \{\mathbf{X} \in \Omega \mid X_1 = X_2\}$. It can be recognized that the hexahedral discretization based on $\mathcal{S}_{\text{HEX}}$ is heavily polluted by a spurious pressure mode (checkerboard mode). It can be seen in Fig. 6c that the severity of the pressure mode increases towards the center of the domain. From these results, one can conclude that the pressure distributions of Figs. 6a–c are physically unreasonable and cannot be used without extensive post-processing of the spurious pressure modes. This once more indicates that the H1/P0 element must be used with care and is generally unreliable if the pressure or the stress are the quantities of interest.

Since the discretization based on the set $\mathcal{S}_{\text{HCB}}$ fulfills the topological requirements to suppress spurious modes, the pressure plots of Figs. 6d–f are free of spurious pressure modes. The results show that the pressure distribution is reasonable, smooth and symmetric. The absence of a checkerboard mode leads to a maximum absolute pressure which is almost 14 times smaller than on the hexahedral mesh.

Another indicator for the fulfillment of the inf-sup condition on a non-degenerate Voronoi mesh can be provided by the inf-sup test [28]. The inf-sup constant β_h is evaluated numerically by an equivalent eigenvalue problem for a collection of meshes with increasing degree of refinement. The square root of the smallest non-zero eigenvalue corresponds to the discrete inf-sup constant β_h and must be bounded away

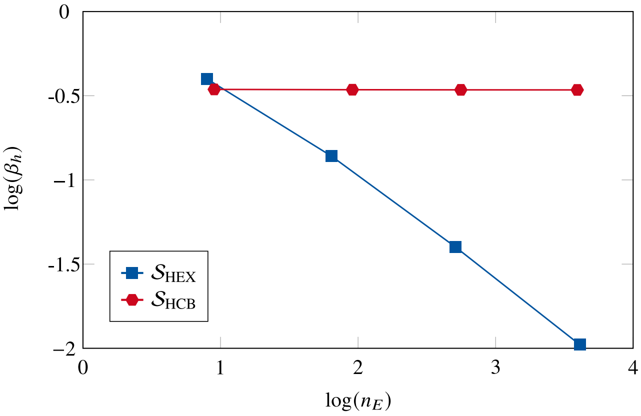

Fig. 7 Lid-driven cavity. Evaluation of the discrete inf-sup constant β_h using the numerical inf-sup test [28] for the set $\mathcal{S}_{\text{HEX}}$ with $N = 2, 4, 8$ and 16 and the set $\mathcal{S}_{\text{HCB}}$ with $M = 1, 3, 6$ and 12

from zero to pass the test. The results of the inf-sup test are shown in Fig. 7. The discrete inf-sup constant β_h is

evaluated on the hexahedral mesh based on $\mathcal{S}_{\text{HEX}}$ with $N = 2, 4, 8$ and 16, and on the bitruncated cubic honeycomb mesh based on $\mathcal{S}_{\text{HCB}}$ with $M = 1, 3, 6$ and 12. The results confirm that the H1/P0 element does not pass the inf-sup test, since β_h decreases steadily towards zero for increasing values of N. Using the lowest-order polyhedral finite element formulation on the honeycomb mesh delivers an inf-sup constant which is almost independent of M, indicating that the inf-sup test is passed.

4.2 Bridge bearing

To present a practical example considering large deformations, an elastomeric bridge bearing of Glacier GmbH - Sollinger Hütte is considered (see Fig. 8). The top and side views including the most important dimensions are given in Fig. 9. Note that the dimensions of the bearing are given in mm. We will, however, consider consistent units in this example and therefore omit all units for convenience. Since the steel attachment plates are excessively stiff compared to the nearly-incompressible elastomeric block, it is assumed that both plates are rigid. The lower attachment plate is considered fully fixed to the substructure, while the upper plate, attached to the superstructure, can only move in the horizontal plane. There is no relative displacement between the elastomer and the attachment plates. A more detailed version of this problem—modeling both the attachment plates and the elastomer—can be found in [53].

For the elastomer, a nearly-incompressible Neo-Hookean material law with the deviatoric strain energy density function

$$W_{\text{dev}} = \frac{\mu}{6}\left(3\operatorname{tr}(\mathbf{C}) - 4\ln(J) - J^2 - 8\right). \tag{66}$$

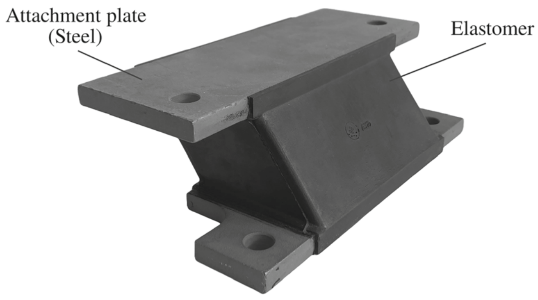

Fig. 8 Bridge bearing containing the elastomeric block and the attachment plates

is chosen with $\mu = 2.1125 \cdot 10^{-3}$. The Lamé constant $\lambda = 100$ leads to the Poisson's ratio $\nu = 0.499989$ and implies nearly-incompressible material behavior, which is enforced by the penalty function $\hat{U} = J - 1$ of Eq. (2). To reduce the numerical effort, the symmetry of the problem is taken into account and only half of the domain is discretized. Appropriate symmetry boundary conditions are therefore set on the hyperplane $\{\mathbf{X} \in \Omega \mid X_1 = 105\}$. To investigate the occurrence of a spurious pressure mode, a shear deformation corresponding to the component's maximum allowed relative displacement of 44 is applied in both positive and negative X_2-directions. Nonhomogeneous Dirichlet boundary conditions with magnitudes

(A) $\bar{u}_2\,(X_3 = 58) = +44$, and
(B) $\bar{u}_2\,(X_3 = 58) = -44$

are therefore prescribed on the upper boundary of the elastomeric block, while the X_1-components remain unconstrained. We consider the following three finite element meshes:

1. A regular hexahedral mesh (HEX), dividing the geometry into 10 × 12 × 8 elements whose geometry is similar to the geometry of the domain (see Fig. 10a). In the interior of this mesh, we observe $d_E = 8$, and therefore, spurious pressure modes are expected. The H1/P0 element is used to approximate the solution.
2. An extruded Voronoi mesh (EXT) constructed by the extrusion of a planar mesh in the X_1-direction (see Fig. 10b). In the direction of extrusion, 10 elements are generated. The planar mesh is a centroidal Voronoi mesh in the X_2X_3-plane consisting of 96 elements. Before the extrusion, the planar Voronoi mesh is relaxed using 1000 Lloyd iterations. In this mesh, 6 elements intersect in an interior vertex ($d_E = 6$). The mixed polyhedral finite element formulation of Sec. 2 is used to approximate the solution.
3. A centroidal Voronoi mesh (CTR) constructed by placing 960 random Voronoi sites in the 3D domain (see

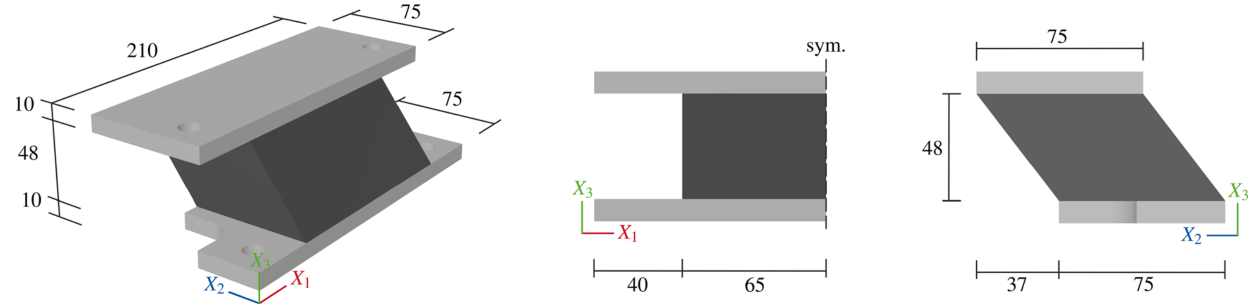

Fig. 9 Bridge bearing. Dimensions of the original problem [53]

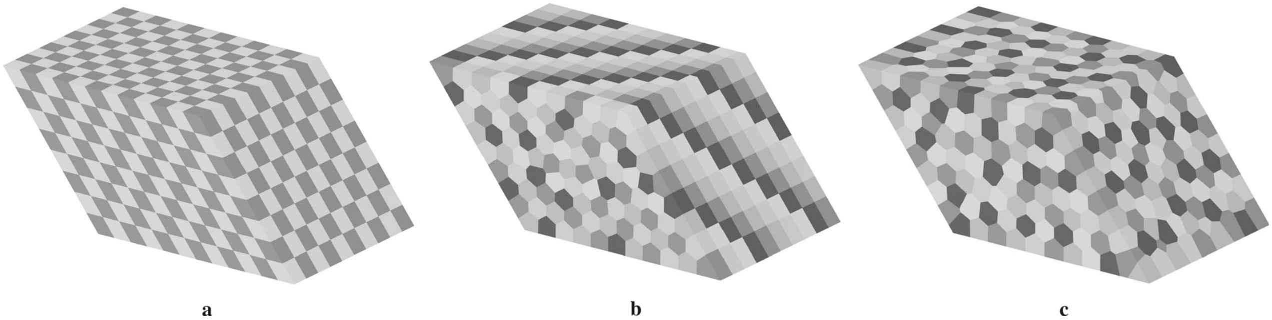

a b c

Fig. 10 Bridge bearing. **a** Hexahedral mesh (HEX) with 12 × 8 × 10 elements. **b** Extruded Voronoi mesh (EXT) created by extrusion of 96 2D centroidal Voronoi elements in the X_1-direction. **c** Centroidal Voronoi mesh (CTR) containing 960 polyhedral elements

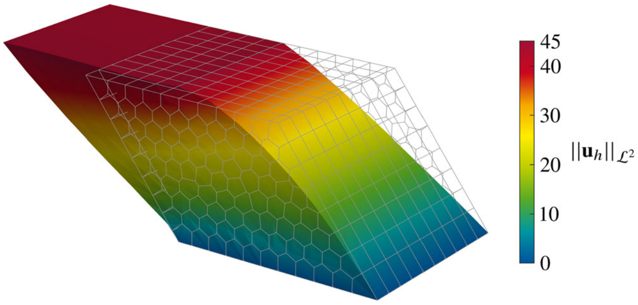

Fig. 11 Bridge bearing. Deformed configuration of the extruded mesh with contour plot of the displacement norm

Fig. 10c). Additionally, 1000 Lloyd iterations are carried out in order to enhance the quality of the mesh. The mixed polyhedral finite element formulation of Sec. 2 is used to approximate the solution.

It is important to mention that the displacement fields calculated on all three meshes deliver practically identical results. For the sake of completeness, the deformed extruded mesh corresponding to load case (A) is shown in Fig. 11 and is in agreement with the deformed configuration shown in [53]. Additionally, we visualize the displacements in 2D by slicing the domain with the hyperplane

$$\mathcal{P}_3 = \{\mathbf{X} \in \Omega \mid 48X_2 - 37X_3 = 1950\}.$$

The displacements of the hexahedral mesh and the centroidal Voronoi mesh on $\mathcal{P}_3$ are shown in Fig. 12. It is shown that there are no distinct differences between the H1/P0 element on the hexahedral mesh and the polyhedral finite element formulation on the centroidal Voronoi mesh.

The pressure solution, on the other hand, shows distinct differences between the three meshes. A 3D visualization of the discrete pressures corresponding to load case (A) can be found in Fig. 13. As expected, spurious pressure oscillations occur in the discrete solution field. One can recognize in Fig. 13a that the pressure field evaluated on the hexahedral mesh exhibits severe checkerboarding, which develops especially in the X_2X_3-plane. In several elements, the superimposition of the spurious pressure mode with the true pressure field causes the pressure to be close to zero. In the X_1X_3-plane, the pressure solution exhibits only minor checkerboarding, which is hardly recognizable from the contour plot. Because the extruded mesh fulfills the mesh requirements to suppress spurious modes in the X_2X_3-plane (i.e. three elements coincide in a vertex [39]), there is no checkerboard mode in this plane and the pressure results do not show an oscillatory behavior. This is confirmed by the evaluation of all pressures on the line

$$\mathcal{G} = \{\mathbf{X} \in \Omega \mid X_1 = 40,\ X_3 = 58\},$$

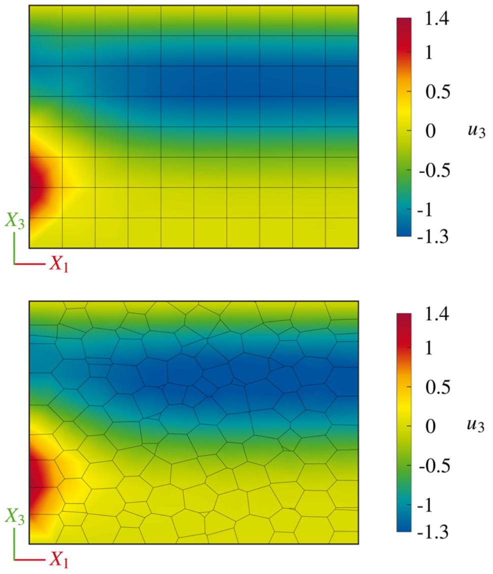

Fig. 12 Bridge bearing. Contour plots of the displacement u_3 for the hexahedral and centroidal Voronoi meshes on the hyperplane $\mathcal{P}_3$

and their graphical representation in Fig. 14. The oscillatory pressure field provided by the H1/P0 element on the hexahedral mesh is visible. One can recognize that the pressures evaluated on the extruded and centroidal Voronoi meshes correspond to the mean values of the pressure field evaluated by the H1/P0 element.

To trigger the spurious pressure mode on the extruded Voronoi mesh, we consider load case (B). The pressure contour plots corresponding to this load case are given in Fig. 15. In Fig. 15a, the superimposed spurious pressure mode is visible. This mode can develop since four elements intersect in a vertex in the X_1X_3-plane, which does not suppress the spurious pressure mode [39]. The pressure distribution on the centroidal Voronoi mesh is smooth but shows slight pressure

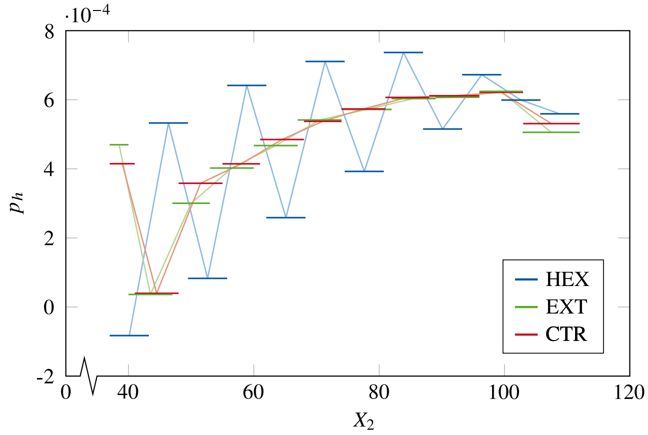

Fig. 14 Bridge bearing. Pressure fields on the line $\mathcal{G}$ for all three considered meshes

jumps around the domains with the maximum and minimum pressures. It is worth mentioning that these are not caused by a spurious pressure mode but occur due to slight irregularities between the neighboring elements. Since a consistent element size is not guaranteed and the centroids of each element are thus arranged in a slightly irregular pattern, the evaluated pressures may be slightly smaller or larger than in their adjacent elements, causing small jumps when cutting along certain lines or planes.

5 Conclusion

In this article, we focused on the inf-sup condition for the lowest-order mixed displacement-pressure finite element formulation in 3D finite elasticity. To fulfill the inf-sup condition and thus suppress spurious pressure modes, a mixed polyhedral finite element formulation, resembling the H1/P0

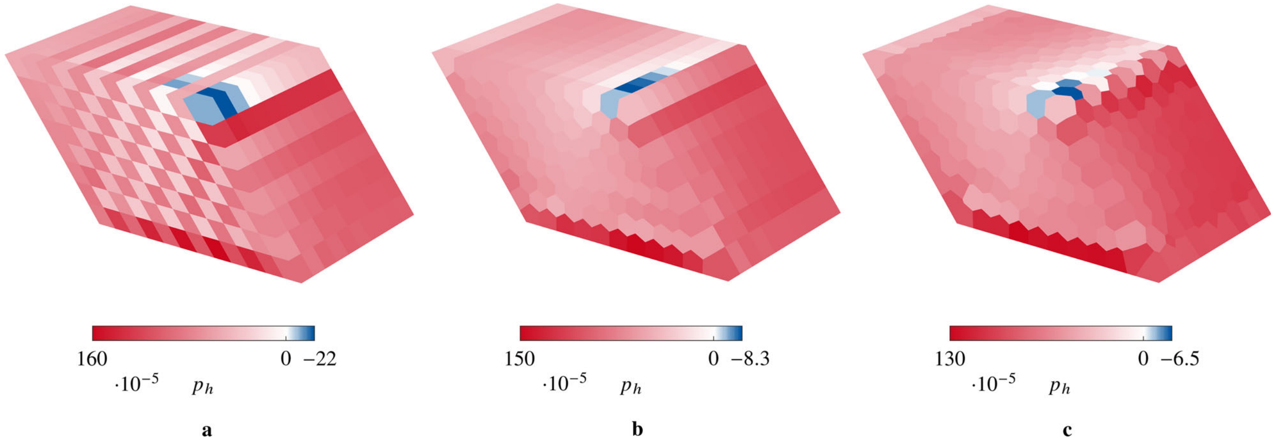

a

b

c

Fig. 13 Bridge bearing. Discrete pressure fields for load case (A). **a** Hexahedral mesh (HEX). **b** Extruded Voronoi mesh (EXT). **c** Centroidal Voronoi mesh (CTR)

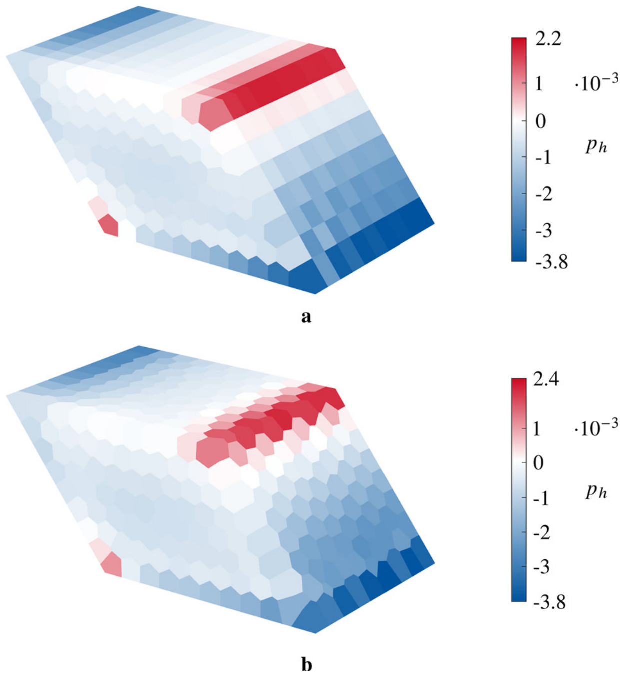

Fig. 15 Bridge bearing. Discrete pressure fields for load case (B). **a** Extruded Voronoi mesh (EXT). **b** Centroidal Voronoi mesh (CTR)

element, is derived. The element is stabilization-free and uses the same variational framework as the H1/P0 element. Since these elements allow us to discretize any type of mesh, the necessary topological mesh requirements are derived to guarantee stability. It is then possible to construct finite element meshes that suppress spurious pressure modes. To conclude, it was shown that:

1. The H1/P0 element is inf-sup unstable and delivers oscillatory pressure results. All spurious pressure modes are derived on a regular hexahedral mesh using the nullspace method.
2. The hydrostatic pressure mode is the only nullspace vector if no more than four finite elements intersect in a vertex. Since this mode does not occur in the solution if a well-posed finite element problem is considered, the pressure field is stable.
3. Non-degenerate Voronoi meshes fulfill the aforementioned property. It is important to select the Voronoi sites with care or use random sampling to avoid degenerate meshes that do not fulfill the requirement.
4. The numerical examples support the derivation and show that spurious pressure solutions only occur if the necessary mesh topology requirements are not met.
5. Using the numerical inf-sup test, it is shown once more that (1), (2) and (3) are fulfilled.

Funding Open Access funding enabled and organized by Projekt DEAL. Funding was provided by Deutsche Forschungsgemeinschaft (Grant No. 495926269).

Declarations

Conflict of interest The authors have no financial or proprietary interests in any material discussed in this article.

References

1. Holzapfel Gerhard A (2002) Nonlinear solid mechanics: a continuum approach for engineering science. Wiley, Chichester
2. Bendsoe MP, Sigmund O (2003) Topology optimization: theory, methods, and applications. Springer, New York
3. Wriggers P, Laursen TA (2006) Computational contact mechanics. Springer, New York
4. Neilan M, Otus BM (2023) A stable and H^1-conforming divergence-free finite element pair for the Stokes problem using isoparametric mappings. Calcolo 60(3):37
5. Hanot Marien-Lorenzo (2023) An arbitrary order and pointwise divergence-free finite element scheme for the incompressible 3D Navier-Stokes equations. SIAM J Numer Anal 61(2):784–811
6. Shamim MB, Wulfinghoff S (2024) Variational three-field reduced order modeling for nearly incompressible materials. Comput Mech
7. Böhm C et al (2023) Mixed virtual element formulations for incompressible and inextensible problems. Comput Mech 72(6):1141–1174
8. Sauren B et al (2023) A mixed polygonal finite element formulation for nearly-incompressible finite elasticity. Comput Methods Appl Mech Eng 403:115656
9. Sauren B, Klarmann SC, Klinkel S (2022) A mixed finite element formulation for arbitrary element geometries and nearly-incompressible finite elasticity
10. Wriggers P et al (2017) Efficient virtual element formulations for compressible and incompressible finite deformations. Comput Mech 60:253–268
11. Wriggers P, De Bellis ML, Hudobivnik B (2021) A Taylor-Hood type virtual element formulations for large incompressible strains. Comput Methods Appl Mech Eng 385:114021
12. Jabareen M (2020) A polygonal finite element formulation for modeling nearly incompressible materials. Meccanica 55(4):701–723
13. Chi H et al (2015) Polygonal finite elements for finite elasticity. Int J Numer Methods Eng 101(4):305–328
14. Madadi AA (2024) A subdivision-stabilized B-spline mixed material point method. Comput Methods Appl Mech Eng 418:116567
15. Chandra B et al (2024) Stabilized mixed material point method for incompressible fluid flow analysis. Comput Methods Appl Mech Eng 419:116644
16. Kikis G, Klinkel S (2022) Two-field formulations for isogeometric Reissner-Mindlin plates and shells with global and local condensation. Comput Mech 69:1–21
17. Alvin C, Sukumar N (2024) Stress-hybrid virtual element method on quadrilateral meshes for compressible and nearly-incompressible linear elasticity. Int J Numer Methods Eng
18. Bombarde DS et al (2022) Hellinger-Reissner principle based stress-displacement formulation for three-dimensional isogeometric analysis in linear elasticity. Comput Methods Appl Mech Eng 394:114920
19. Viebahn N, Steeger K, Schröder J (2018) A simple and efficient Hellinger-Reissner type mixed finite element for nearly incompressible elasticity. Comput Methods Appl Mech Eng 340:278–295

20. Viebahn N, Schröder J, Wriggers P (2019) An extension of assumed stress finite elements to a general hyperelastic framework. Adv Model Simul Eng Sci 6:1–22
21. Schröder J et al (1997) A physically nonlinear dual mixed finite element formulation. Comput Methods Appl Mech Eng 144(1–2):77–92
22. Lamperti A et al (2023) A Hu-Washizu variational approach to self-stabilized virtual elements: 2D linear elastostatics. Comput Mech 71(5):935–955
23. Pfefferkorn R (2023) Hourglassing-and locking-free mesh distortion insensitive Petrov-Galerkin EAS element for large deformation solid mechanics. Int J Numer Methods Eng 124(6):1307–1343
24. Ladyzhenskaya OA (1969) The mathematical theory of viscous incompressible flow
25. Babuška I (1973) The finite element method with Lagrangian multipliers. Numer Math 20(3):179–192
26. Brezzi F (1974) On the existence, uniqueness and approximation of saddle-point problems arising from Lagrangian multipliers. Publ Math Inform Rennes S4:1–26
27. Bathe K-J (2006) Finite element procedures
28. Chapelle D, Bathe K-J (1993) The inf-sup test. Comput Struct 47(4–5):537–545
29. Krischok A, Linder C (2019) A generalized inf-sup test for multi-field mixed-variational methods. Comput Methods Appl Mech Eng 357:112497
30. Sani RL et al (1981) The cause and cure (?) of the spurious pressures generated by certain FEM solutions of the incompressible Navier-Stokes equations. Int J Numer Methods Fluids 1(1):17–43
31. Lee RL, Gresho PM, Sani RL (1979) Smoothing techniques for certain primitive variable solutions of the Navier-Stokes equations. Int J Numer Methods Eng 14(12):1785–1804
32. Sani RL et al (1981) The cause and cure (!) of the spurious pressures generated by certain FEM solutions of the incompressible Navier-Stokes equations: part 2. Int J Numer Methods Fluids 1(2):171–204
33. Nemer R et al (2021) Stabilized finite element method for incompressible solid dynamics using an updated Lagrangian formulation. Comput Methods Appl Mech Eng 384:113923
34. Castañar I, Baiges J, Codina R (2020) A stabilized mixed finite element approximation for incompressible finite strain solid dynamics using a total Lagrangian formulation. Comput Methods Appl Mech Eng 368:113164
35. Rüberg T, Cirak F (2012) Subdivision-stabilised immersed b-spline finite elements for moving boundary flows. Comput Methods Appl Mech Eng 209:266–283
36. Li Y, Zikatanov LT (2022) New stabilized P1× P0 finite element methods for nearly inviscid and incompressible flows. Comput Methods Appl Mech Eng 393:114815
37. Yun G, Lee J, Kim D-N (2023) Stability of mixed overlapping elements in incompressible analysis. Comput Methods Appl Mech Eng 412:116104
38. Taylor C (1973) A numerical solution of the Navier-Stokes equations using the finite element technique. Comput Fluids 1(1):73–100
39. Sauren B, Klinkel S (2023) On the stability of mixed polygonal finite element formulations in nonlinear analysis. Int J Numer Methods Eng 125:e7358
40. Da Veiga LB, Lipnikov K (2010) A mimetic discretization of the Stokes problem with selected edge bubbles. SIAM J Sci Comput 32(2):875–893
41. Klinkel S, Reichel R (2019) A finite element formulation in boundary representation for the analysis of nonlinear problems in solid mechanics. Comput Methods Appl Mech Eng 347:295–315
42. Chongmin Song (2018) The scaled boundary finite element method: introduction to theory and implementation. John Wiley & Sons, New York
43. Schröder J et al (2017) On the stability analysis of hyperelastic boundary value problems using three-and two-field mixed finite element formulations. Comput Mech 60:479–492
44. Auricchio F et al (2013) Approximation of incompressible large deformation elastic problems: some unresolved issues. Comput Mech 52:1153–1167
45. Auricchio F et al (2017) Mixed finite element methods. In: Encyclopedia of computational mechanics, 2nd edn. pp 1–53
46. Dvorkin EN (2001) On the convergence of incompressible finite element formulations: the patch test and the inf-sup condition. Eng Comput 18(3/4):539–556
47. Benzi M, Golub GH, Liesen J (2005) Numerical solution of saddle point problems. Acta Numer 14:1–137
48. Mario B et al (2010) Polygon mesh processing. CRC Press, Boca Raton
49. Lloyd S (1982) Least squares quantization in PCM. IEEE Trans Inform Theory 28(2):129–137
50. da Beirão Veiga L et al (2013) Basic principles of virtual element methods. Math Models Methods Appl Sci 23(01):199–214
51. Chi H et al (2020) Virtual element method (VEM)-based topology optimization: an integrated framework. Struct Multidiscip Optim 62(3):1089–1114
52. Wriggers P, De Bellis ML, Hudobivnik B (2021) A Taylor-Hood type virtual element formulations for large incompressible strains. Comput Methods Appl Mech Eng 385:114021
53. Klinkel S (2000) Theorie und Numerik eines Volumen-Schalen-Elementes bei finiten elastischen und plastischen Verzerrungen. Inst für Baustatik